A NEW TYPE OF MAGNET ARRAY

FOR PLANAR MOTOR

by

Rui Chen

B.A.Sc., Huazhong University of Science and Technology, 2000

M.A.Sc., Huazhong University of Science and Technology, 2003

A THESIS SUBMITTED IN PARTIAL FULFILLMENT OF

THE REQUIREMENTS FOR THE DEGREE OF

MASTER OF APPLIED SCIENCE

in

THE FACULTY OF GRADUATE AND POSTDOCTORAL STUDIES

(Mechanical Engineering)

THE UNIVERSITY OF BRITISH COLUMBIA

(Vancouver)

December 2016

Abstract

Non-contact 6-DOF planar motors are playing more and more important roles in high precision machine tools, such as photolithography machines in semiconductor industry. Among existing planar motor designs, magnetically levitated planar motors with moving magnet have the potential to greatly improve the performance of motion stages by eliminating the force disturbance from umbilical cables and hoses that supply electricity and cooling water to motion stages, and can be easily extended to multiple-stage application. However, moving magnet planar motors suffer from intrinsic high-order force ripples that are generated by the interaction between stator coils and magnetic field harmonic components from magnet arrays. This thesis presents the design, analysis and experimental results of a novel magnet array for planar motor application, termed as M-Magnet array.

An M-Magnet array consists of four identical magnet pieces per spatial period. Each magnet piece has a magnetization axis in 45 degree direction relative to its side surfaces, instead of 0 or 90 degree magnetization pieces used in conventional Halbach arrays. To minimize force disturbance generated in orthogonal coils, symmetric magnet arrays are preferred. Previous symmetric magnet array contains 5 magnet pieces at each spatial period with the two edge pieces having half width of inner magnet pieces. The new M-magnet array design allows a symmetric magnet array made of 4 identical pieces. In addition, M-Magnet array design has the scalability to be extended to various sizes of mover with only one type of magnets, which makes the manufacturing of movers more cost effective. This thesis develops 3D analytical models to investigate the actuating force and torque generation of magnet arrays, and its sensitivity to

manufacturing tolerances. The results indicate that the motor performance is relatively insensitive to manufacturing tolerance.

For high precision positioning applications, force and torque characteristics of the planar motor are desired to be highly linear and less intrinsic force disturbance in order to minimize control effort. A novel hybrid array design based on M-Magnet array is presented which can attenuate 6^{th} force ripple by a factor of 100 without sacrifice of force constant of the planar motor compared to existing array splitting solution. The new M-Magnet array and hybrid array designs are analyzed via 2D and 3D models.

An M-Magnet array is fabricated and experimentally tested at two distances from the magnet array bottom plane. The experimental results match the calculation results from 3D analytical models within 3% deviation, which confirms the validity of the 3D models.

Preface

The work in this thesis has been carried out at the Precision Mechatronics Laboratory (PML), Department of Mechanical Engineering, under the supervision of Dr. Xiaodong Lu. The conceptual ideal of M-Magnet array originally came from Dr. Xiaodong Lu.

Chapter 1 is the introduction and a brief literature review of existing magnet array pattern for planar motor applications. Figures 1-1, 1-2, 1-5a, 1-5b, 1-6a, 1-6b, 1-7 and 1-8 are cited from literature, as noted by each figure. Figures 1-5c and 1-6c are the author's calculation results for existing designs in published patents as noted under the figure.

Chapter 2 is the calculation theories for analyzing M-Magnet arrays. All these theories are developed based on previous work from published papers.

Chapter 3 is the design and calculation of M-Magnet array. All calculation methods and coding of M-Magnet arrays are performed by the author.

Chapter 4 is the experiment results of an M-Magnet array. The magnet array was assembled by the author and the experiments were also carried out by the author.

Table of Contents

List of Tables

List of Figures

List of Abbreviations

1-D	One Dimensional
2-D	Two Dimensional
6-D	Six Dimensional
DOF	Degrees Of Freedom
PCB	Printed Circuit Board
NS	North and South
RMS	Root Mean Square
FEM	Finite Element Model
EQS	Electro-Quasi-Static
MQS	Magneto-Quasi-Static
CG	Center of Gravity
MGOe	Mega Gauss Oersteds
IC	Integrated Circuit

Acknowledgements

I wish to thank in particular my supervisor, Dr. Xiaodong Lu, who gave me the chance to go back university to do research again. He is always supportive when I am feeling frustrated about the courses and researches. He is always available to answer questions with patience and humor. Together, we had a lot of fun in the research.

I thank my previous and current labmates: Mark Dyck, Irfan-ur-rab Usman, Keir Maguire, Eric Buckley and Jian Gao. Mark gave me a very wonderful introduction about his project and that was the first time I knew that the planar motor can not only move back and forth, but also play music as a speaker. Irfan helped me getting involved in the lab quickly. Let me feel like I am a new family member of PML. Eric invited me to the camp trip at Harrison Lake. That was the first time I saw how beautiful Canada is with my own eyes. Keir invited me to his birthday party and many other parties and helped me to practice English. Jian helped me to pick up my wife and daughter and move to new home. All of these will be my precious memories.

Special thanks are owed to my wife, my daughter and my parents. Whenever I make big decisions in my life, such as quitting the job or going abroad for studying after working for a long time, they are always being with me, encouraging me and supporting me. Especially, my wife sacrificed her career to go abroad with me and so much free time to take care of my daughter and me when I was busy at home works, exams, researches and thesis.

For my wife, my daughter and my parents.

Chapter 1: Introduction

Driven by Moore's law, minimum feature size of integrated circuit (IC) is decreasing from several micrometers in 1970's to slightly over 10 nanometers nowadays. Lithography tool, one of the most important machines in Semiconductor industry, plays a leading role to support Moore's law. A key component of lithography tool is wafer stage, which positions a wafer under a lens-system. To satisfy severe performance demands in terms of speed and accuracy, wafer stage keeps evolving from conventional mechanical contact stage to non-contact air bearing stage [1][2][3], latterly to the state of the art magnetically non-contact stage with moving coils [4][5][6]. Now more and more researches focus on magnetically levitated stage with moving magnet [7][8][9][10][11][12], which could be a new solution to further improve the performance of wafer stage. Generally, speed and accuracy are in conflict with each other on the design of motion control device such as wafer stage. One of the major trouble makers is high-order force ripples from actuator of the stage, which are position dependent and will degrade the performance as speed going up. This thesis presents a new type of magnet array for magnetically non-contact stage to simplify mover design and effectively attenuate force ripples.

1.1 Thesis Overview

This thesis is divided into five main parts:

Chapter 1: Introduction

This chapter introduces the motivation of the thesis and presents the background of planar motor in high precision machine. Previous magnet array designs for planar motor are reviewed.

Chapter 2: Theory of Electromagnetic Field Analysis

This chapter presents two approaches for magnet field modeling, 2D Fourier series model and 3D magnetic surface charge model. Forces and torques generated by conventional Halbach array interacting with stator coils are calculated based on analytical models.

Chapter 3: Novel M-Magnet Array Design for Planar Motor

This chapter shows the new magnet array design in terms of magnetizing pattern and array layout for 2D and 6D actuations, and investigates the relationship between manufacturing error and planar motor performance to demonstrate its manufacturing feasibility that performance is relatively insensitive to manufacturing tolerance.

Chapter 4: Experiment

This chapter describes the experiment set-up for testing the magnetic field of an M-Magnet array at different distances from bottom surface of magnet array. The experimental results are presented and analyzed.

Chapter 5: Conclusion

This chapter summarizes the contribution of this thesis and discusses future work.

1.2 Thesis Contribution

The main contributions of this work are:

- Design and manufacture of a novel M-Magnet array for magnetically levitated planar motor application.
- Design a novel hybrid array based on M-Magnet array to eliminate 6^{th} force ripple generated by magnetic field harmonics interacting with orthogonal coils.
- Modeling and analyzing the 3D field and harmonics of M-Magnet array and hybrid array.
- Investigate the relationship between manufacturing tolerances and actuation performance of M-Magnet array to demonstrate its manufacturing feasibility.

- Assemble M-Magnet arrays and build experimental set-up to test magnetic field for validation of M-Magnet array design

1.3 Stage Architectures for High Precision Machine

For several decades, there has been much research into nano-scale high-precision systems for wafer stage in semiconductor industry. Six degrees of freedom (DOF) are typically required for this kind of machine. X-Y planar motion is for transporting wafer from one work station to another, whereas other four short axes are used to align wafer with other devices of lithography tool. Conventional two-dimensional motion control devices using a mechanical transformer, such as a gear or ball screw, are faced with the difficulty of very precise position control. Furthermore, dust particle and heat caused from wear of contacts and friction are unacceptable in clean room environment. Therefore, they are obsolete and replaced by non-contact actuating systems. Generally, there are two classes of non-contact actuating solutions for high precision applications: i) direct drive linear motor combined with high pressure air bearing to guide planar motion [1-3]; ii) planar motor [5-12] inherently has the ability to levitate using magnetic force coming from electromagnets or permanent magnets. For maglev planar motor, it can be also categorized as moving coil planar motor and moving magnet planar motor.

1.3.1 Linear Drive Stage with Air Bearing

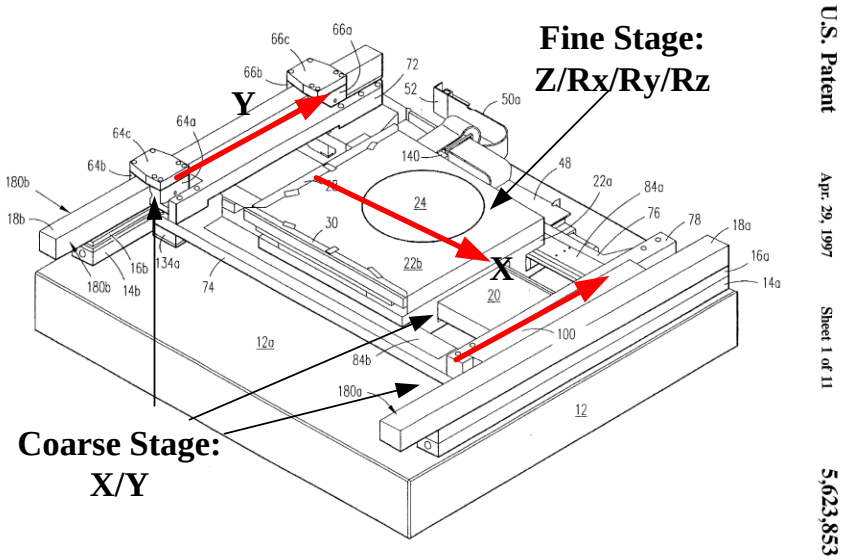

Figure 1-1 H-drive style single stage, figure taken from [1]

Figure 1-1 shows a widely adopted H-drive style single stage [1] in semiconductor manufacturing, including lithography, wire bonding, wafer metrology, packaging and so on. At least three layers of motion elements are clumsily stacked. Y axis stands on granite as bottom carrier with X axis sitting on it. Both X and Y axes constitute the coarse stage. With 4DOF fine stage stacking on top of the coarse stage, 6DOF motion stage is obtained. Aerodynamic bearing exerting on Y axis can achieve easy, stiff and stable levitation and position control, but it cannot be used in a vacuum environment which is common in semiconductor industry. In addition, scalability is another problem for this stage. It's very difficult to extend from single stage to multiple stages due to the constraint of the guide providing air bearing. Multiple stage configurations are also becoming more and more popular in lithography tools, which can dramatically improve the throughput of the tool.

1.3.2 Maglev Stage with Moving Coil Planar Motor

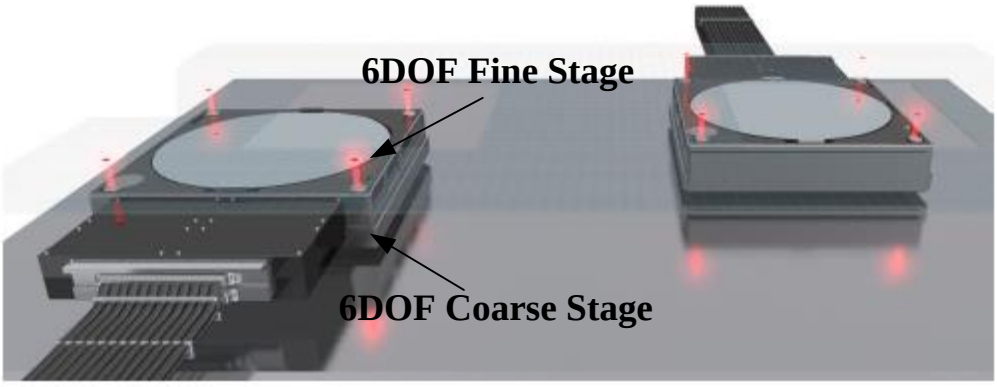

Figure 1-2 Maglev dual stage with moving coil planar motor, figure taken from [6]

Figure 1-2 shows the state-of-the-art maglev multiple stages, which are integrated in the latest front-end lithography apparatus [6]. 6DOF coarse stage is levitated and driven by a moving coil planar motor inside, which can easily generate around 3g [13] acceleration if the moving coil can be forced cooling appropriately. Guide free architecture provides it with ability to freely move in plane and scalability to multiple stages. However, there are still some disadvantages for this design. Firstly, two layers of motion elements, 6DOF fine stage sitting on 6DOF coarse stage [14] to enhance performance on the end effector, will lead to higher load and constrain accelerating ability. Secondly, umbilical motor cables and cooling hoses of planar motor, which are attached to the mover, will impede free motion of coil assembly; consequently not only moving path of the stage is limited but significant unpredicted disturbance forces are caused. All above problems can be solved by cable-free planar motor with moving permanent magnet (PM).

1.3.3 Maglev Stage with Moving Magnet Planar Motor

Although there is no cable issue for maglev stage with moving magnet, some other questions arise: 1) how to design a stator coil to make force generation easier, smoother and more efficient; 2) how to design magnet array to eliminate force ripples. If these two questions cannot be

answered properly, high precision 6DOF fine stage stacking on the maglev planar motor is inevitable to ensure final performance of the whole system, which means cables issue is only alleviated instead of being eliminated totally to set free of the stage.

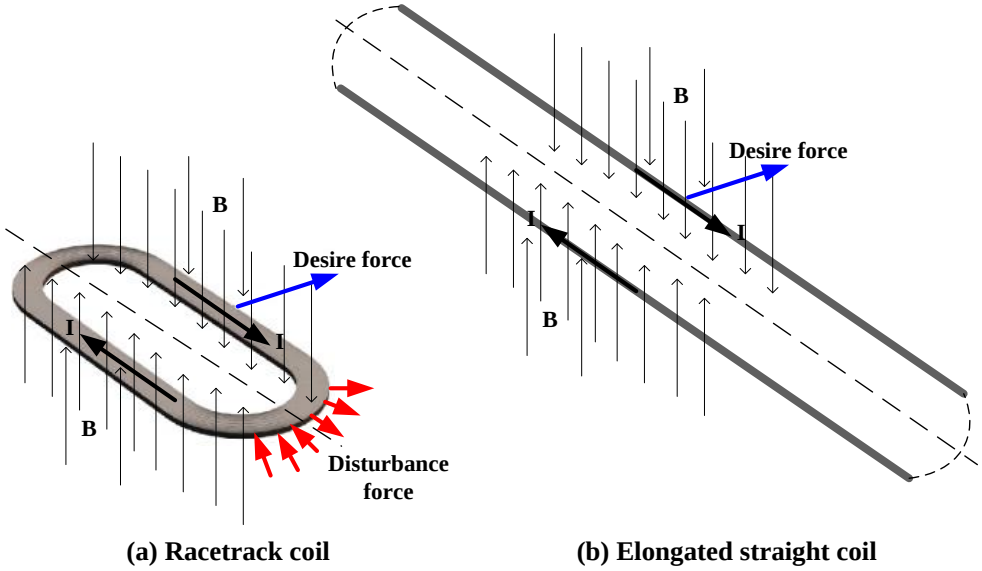

(a) Racetrack coil **(b) Elongated straight coil**

Figure 1-3 Comparison of Racetrack coil and Elongation straight coil

The first problem can be solved by elongated coil pattern in [7][12], which is illustrated in figure 1-3. Most of maglev stages use conventional racetrack coil as building blocks of stator [5][8][9][10][11]. One major issue of racetrack coil is edge effect at two current return ends, which will generate undesired disturbance forces, shown in figure 1-3a. Whereas, a novel stator with elongated straight coil pattern using general printed circuit board (PCB) manufacturing procedure was invented by Xiaodong Lu in 2012, which can effectively eliminate edge effect from current return. The ideal of this new coil pattern is moving current return ends of each coil far away from the magnet field of the mover, depicted in figure 1-3b, thus no disturbance forces will be generated at the current return ends. On the other hand, elongated straight coil pattern has

another benefit that it can get rid of edge effect from magnets as well [15]. This will be discussed in following section.

1.4 Previous Magnet Array for Planar Motor

In general, we can classify planar motor in terms of magnet array pattern: 2D array pattern and 1D array pattern. For each pattern, it also has two classes of magnet array unit, NS array and Halbach array.

1.4.1 Halbach Array vs NS Array

Before going through the discussion of different array pattern, this section will conceptually introduce two types of magnet array units: Halbach array and NS array.

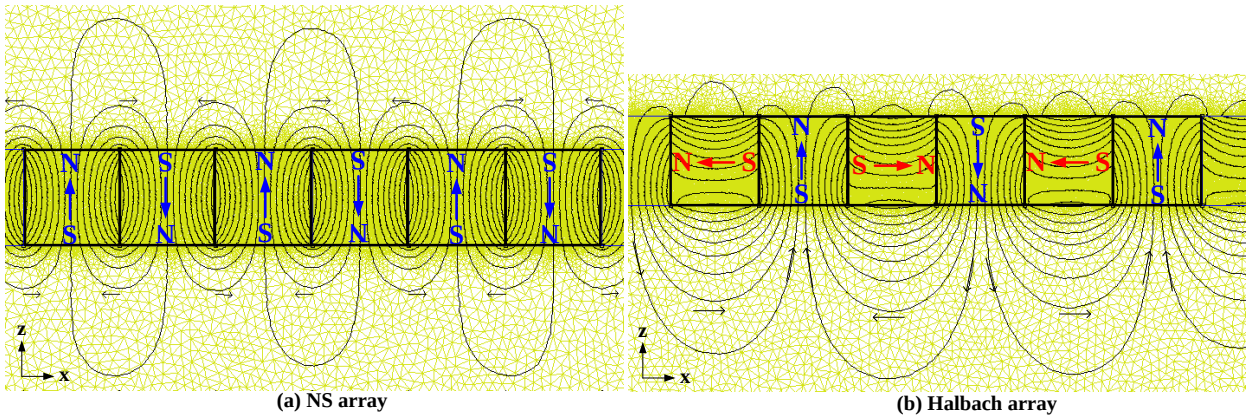

(a) NS array (b) Halbach array

Figure 1-4 Comparison of NS array and Halbach array

NS array in figure 1-4a consists of two magnet components: north component and south component magnetized in +Z and –Z direction respectively, whereas Halbach array in figure 1-4b includes four magnet components instead of two. Another two components are east component magnetized in +X direction and west component magnetized in –X direction other than north and south components. Intuitively, from the finite element simulation, there are two major differences between Halbach array and NS array: 1) Halbach array has field self-shielding effect on topside of array without any back iron, whereas NS array has same field strength on

both sides; 2) On underside of Halbach array, it inherently has much stronger airgap flux density than NS array. From [18], Halbach array is about $\sqrt{2}$ times stronger than NS array. This characteristic is very useful in planar motor design, which can increase force density on strong side to enhance levitation force. More theories about Halbach array will be discussed in chapter 2.

1.4.2 2D Magnet Array

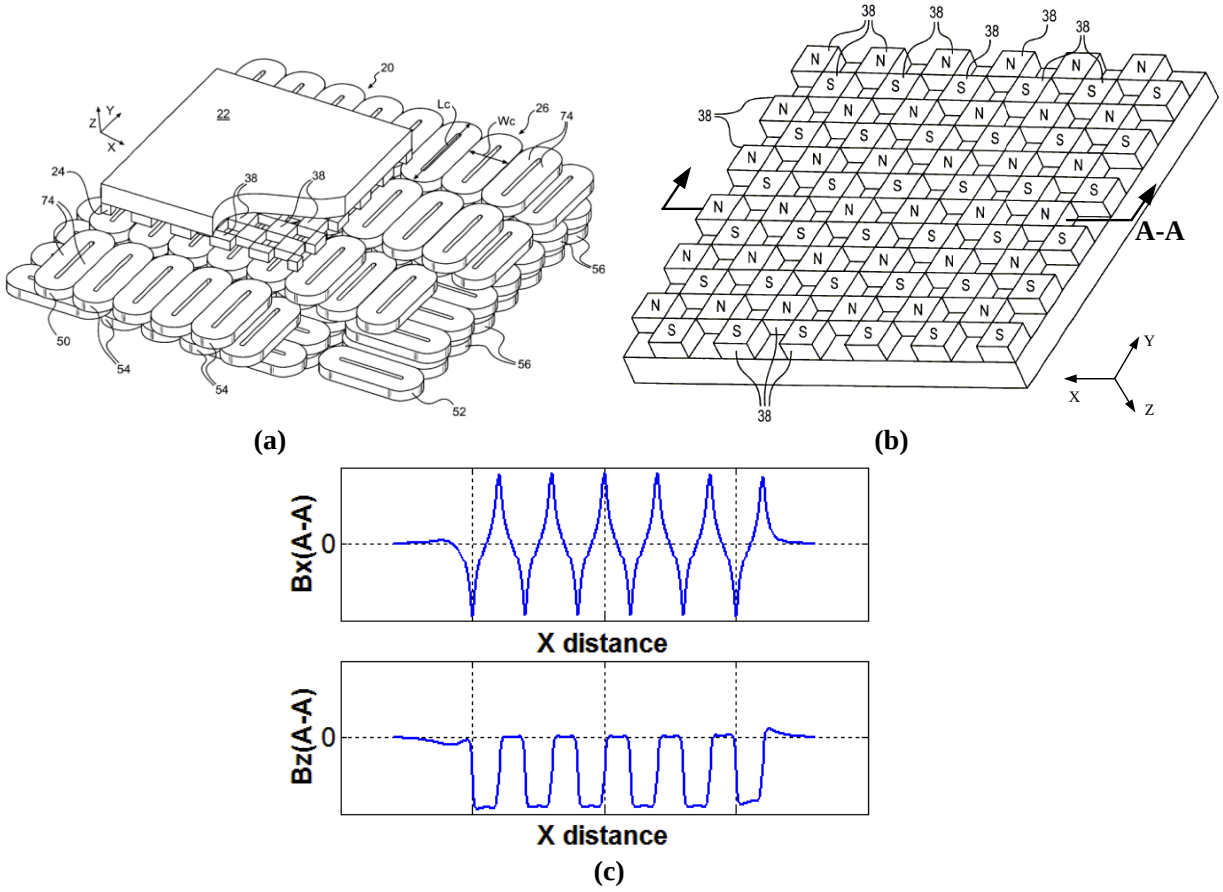

Figure 1-5 Binnard et all. Magnetically levitated 6DOF planar motor (a) Planar motor overview, figure taken from [9]; (b) 2D NS array pattern, figure taken from [9]; (c) Magnet field of Bz and Bx at cross section A-A

Figure 1-5a shows a magnetically levitated 6DOF planar motor presented in 2002 by Binnard et all [9]. For this design, the underside of the mover has a chessboard style 2D NS magnet array,

as shown in figure 1-5b. The racetrack stator coils are stacked layer by layer under the mover to enhance the force constant of the planar motor. However, this will increase the complexity of amplifier due to large number of coils. On the other hand, if we look at the magnet field of the cross section of A-A in figure 1-5b, it's noticed that magnet field in Z direction (Bz) generating thrust force, and magnet field in X direction (Bx) generating levitation force, are non-sinusoidal shape, as shown in figure 1-5c (3D magnetic field simulation is attached in Appendix A.1). This will result in very big position dependent force ripples.

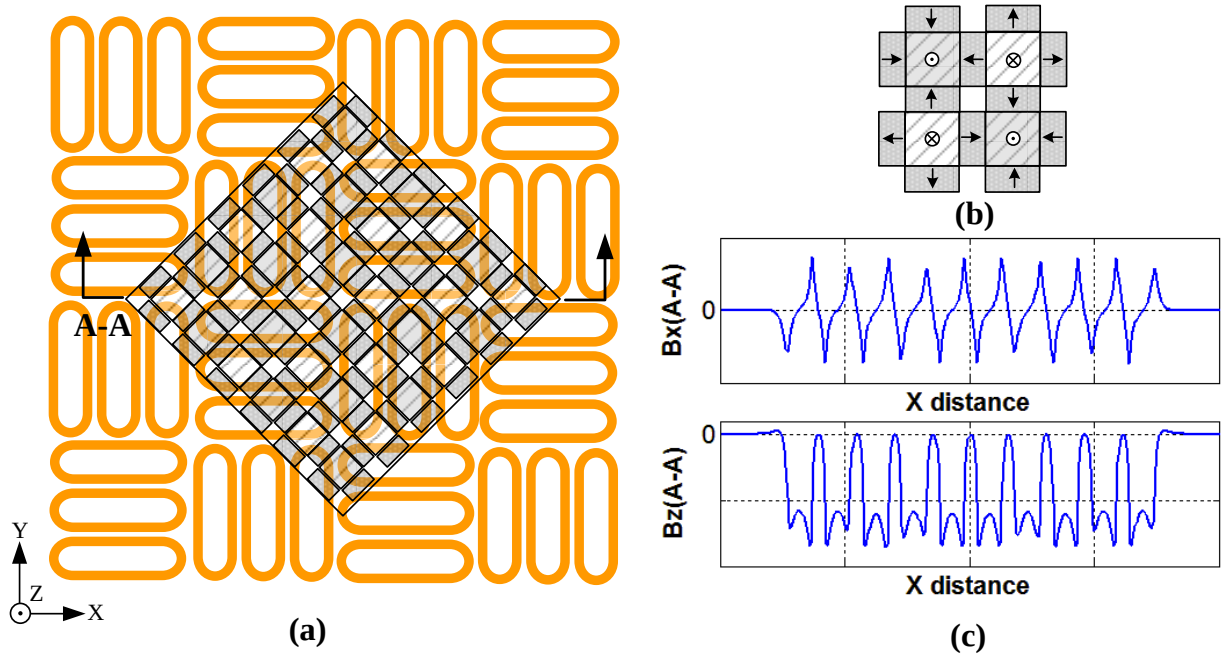

Figure 1-6 Compter et all. 6DOF planar motor (a) Planar motor overview, figure adapted from [11]; (b) 2D Halbach array unit, figure adapted from [11]; (c) Magnet field of Bz and Bx at cross section A-A

Similar design in figure 1-6a was presented by Compter et all. [11] in 2011, which also consists of racetrack stator coils and 2D chessboard style magnet array. However, there is one major difference between these two planar motors about the mover design. For Compter's planar motor, 2D Halbach array is used as building block of the mover, shown in figure 1-6b, instead of

NS array in Binnard's design. This is why magnet array has 45^o angular offset relative to stator coil in figure 1-6a. As discussed in section 1.4.1, Halbach array has two advantages compared to NS array. Firstly, field self-shielding effect on topside of the planar motor could be very useful when it's applied to the stage carrying magnet field sensitive workpiece. On the other hand, strengthened field on the underside of planar motor is a big benefit for motor design, which can enhance the force density of the planar motor. But the disadvantages of Halbach array are also obvious. First of all, if we look at the magnet field at the cross section A-A in figure 1-6a, similarly as the analysis for Binnard's design in figure 1-5b, it's clear that Halbach array has more and much bigger magnetic field harmonics compared to NS array, which is depicted in figure 1-6c (3D magnetic field simulation is attached in Appendix A.2), where Bz and Bx distort even worse with respective to sinusoidal shape field. Furthermore, intrinsic field coupling between X and Y is also stronger than Binnard's design. Finally, more magnet components are required for array assembly compared to NS array.

In sum, all of these designs suffer from force ripples generated by 2D magnet array and position dependent forces as the coils are discrete underneath the magnetic field. The coils also have end turns that are always exposed under the magnetic field, resulting in unwanted force coupling between axes. Although non-sinusoidal current waveforms [16] and mapping decoupling matrix [10] can be applied to attenuate force ripples, this will lead to new problems: i) too much computation effort for real time controller; ii) stage performance will be very sensitive to manufacturing and structure stability.

1.4.3 1D Magnet Array

Instead of using 2D magnet array in moving magnet planar motor, 1D magnet array has two significant advantages: 1) high performance can be easily achieved with less control effort since

no intrinsic coupling between magnet arrays in X and Y directions, and force ripples are much smaller; 2) magnet array assembly is easier compared to 2D array because less magnet pieces are needed. Furthermore, elongated coil pattern can be applied to 1D array, which can easily avoid edge effect at end turns of each coil compared to racetrack coil because they are far away from magnet field. Practically, over half of spatial period of magnet array between end turns and the edge of magnet array is good enough to ensure stage performance since the field decays very fast beyond this distance [17].

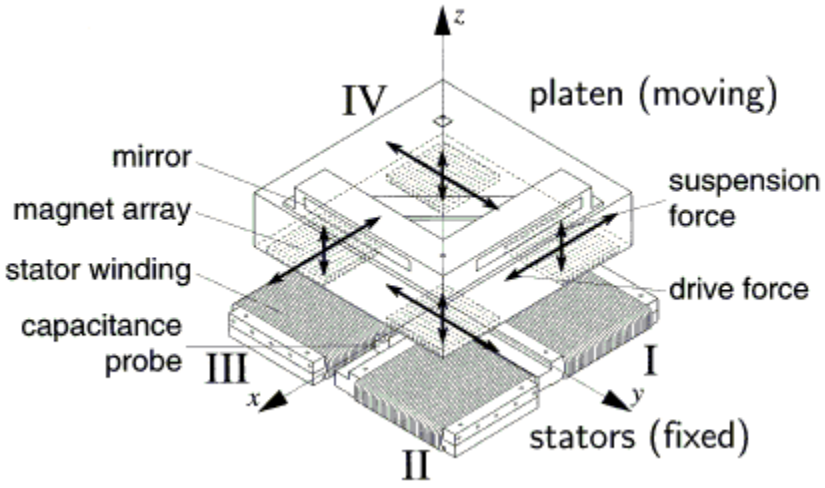

Figure 1-7 Kim's 6D magnetic levitation stage, figure taken from [18]

Kim and Trumper [18] invented a 6DOF "high precision magnetic levitation stage for photolithography" in 1998. There are four single dimension magnetic Halbach arrays mounted on the bottom side of the mover. The stator is made by wire coils separated into four parts, each one under a magnet array respectively. Each coil and magnet array pairs can generate levitation and translation forces, shown in figure 1-7. This is the first stage proving that maglev planar motor with 1D Halbach array can achieve very high performance, 5-nm RMS positioning noise in x and y, 10nm RMS positioning noise in z. However, Kim's stage has a big problem for practical applications: its travelling stroke is coupled with the size of armature, which leads to a

much large footprint if large stroke is required. To solve this problem, Lu and Usman developed a new type of planar motor, as shown in figure 1-8. By using elongated coil pattern manufactured by PCB process, not only high performance of the stage is guaranteed, but more advantages can be achieved compared to Kim's design and racetrack coil pattern designs: 1) very compact and accurate coil layout; 2) high filling factor of stator; 3) very easy to be scaled to large moving range and extended to multiple stages.

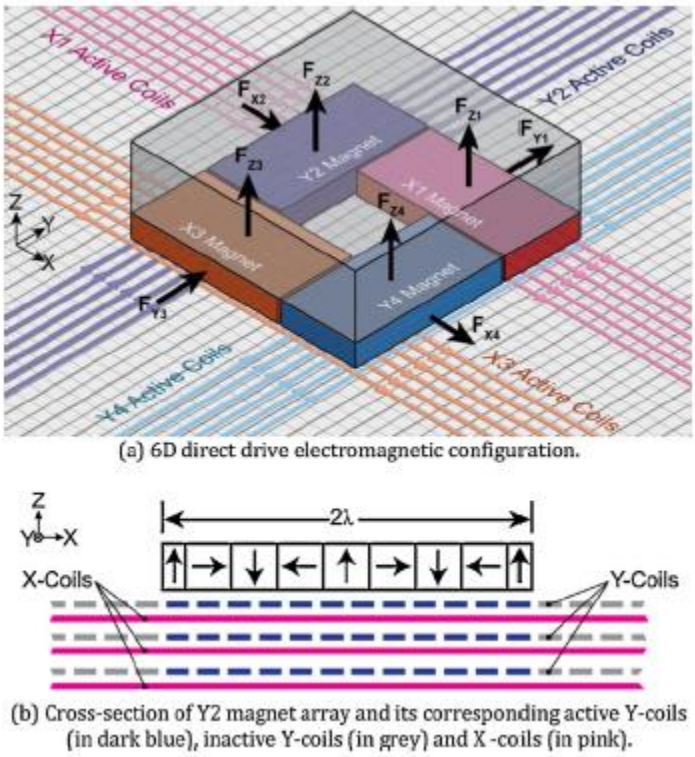

(a) 6D direct drive electromagnetic configuration.

(b) Cross-section of Y2 magnet array and its corresponding active Y-coils (in dark blue), inactive Y-coils (in grey) and X -coils (in pink).

Figure 1-8 Lu's planar motor overview, figure taken from [12]

1.5 Proposed Magnet Array

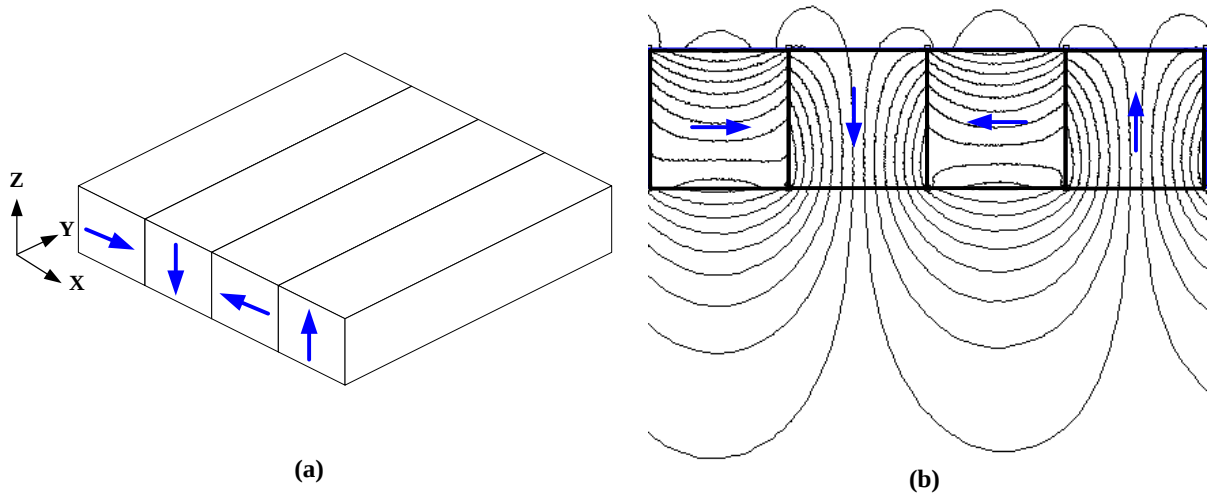

Figure 1-9 Conventional Halbach array

Typically, 1D Halbach array uses four blocks per period, and each block is uniformly magnetized in Y axis. If magnetization axis of each block is either Z or X and rotates by 90^o in each subsequent block, then this specific pattern in figure 1-9a is conventional Halbach array. From finite element solution of conventional Halbach array in figure 1-9b, it's noticed that the field distribution is asymmetric about its vertical middle axis, which will cause disturbance torques if there is current along X direction going through the field. Therefore, in practice, symmetric Halbach array is adopted, as shown in figure 1-8b [12]. This magnet array is also used in the mover design of [18]. There are some drawbacks about symmetric Halbach array: 1) Different size of magnet blocks are needed, five blocks per period instead of four, which will increase the manufacturing cost; 2) Long and thin magnet block makes array assembly very difficult since it's easy to be broken during assembly; 3) 5^{th} harmonic of 1D Halbach array [19] is the source of 6^{th} force ripple when applied to planar motor. Usman uses array splitting method to attenuate 6^{th} force ripple in [20], but this will lead to new problems: a) Splitting gap makes

array assembly even harder; b) Force constant will be reduced by 5% compared to non-splitting array.

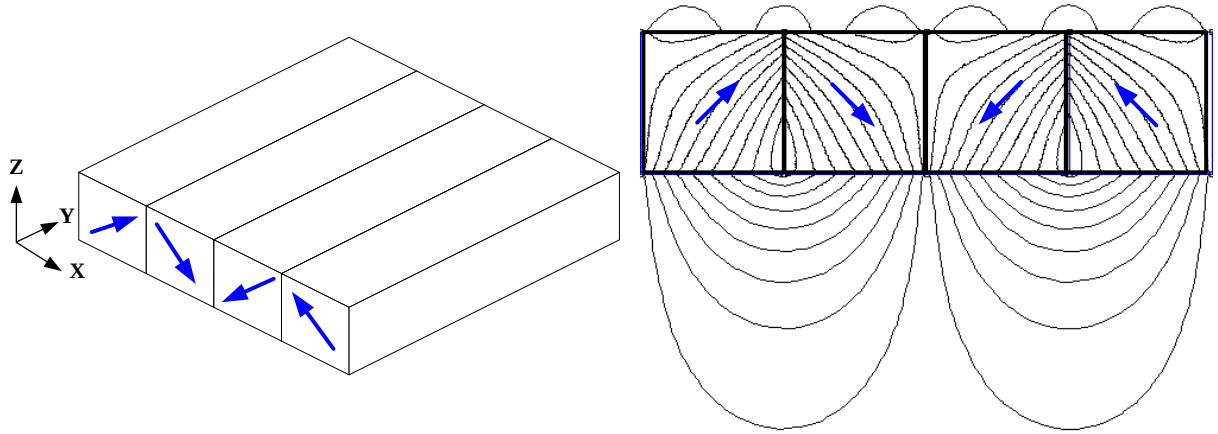

Figure 1-10 M-Magnet array

This thesis will present a novel M shape magnet array consisting of four blocks per period. All blocks are identical with a magnetization axis along 45^o direction relative to its side surface. To start from the left block, rotating by 90^o along clockwise direction in each subsequent block, an M-Magnet array is formed as shown in figure 1-10a. From the finite element solution of an M-Magnet array in figure 1-10b, it's obvious that magnetic field of this new array is mirror-symmetric about vertical middle axis. Hence, only one type of magnet block needs to be fabricated and assembled. Further, if we look at the magnetic flux density of left two blocks in figure 1-10b, attraction force can easily bind these two magnets together, similarly as right two blocks. So we can manipulate one pair of magnets as one group during array assembly. The only assembly effort is how to put two pairs together since repelling force will push against each other. Therefore, assembly process of M-Magnet array can be dramatically simplified compared to symmetric Halbach array, in which repelling forces produced between each magnet piece will make array assembly even harder.

On the other hand, to diminish 6^{th} force ripple due to 5^{th} harmonic of M-Magnet array without sacrifice of force constant, hybrid magnet array layout is presented in this thesis based on M-Magnet array pattern. More details will be discussed in chapter 3.

Chapter 2: Theory of Electromagnetic Field Analysis

Planar motor is a kind of electromagnetic actuator using synchronous commutation law. Typically, the use of 3D finite element (FEM) analysis for evaluation of topologies, design and optimization of the planar motor is inconvenient due to the simulation time. On the other hand, 3D model is too complex for harmonic components analysis of magnet array, which is the key to investigate the force ripples of planar motor. In this chapter, theories that govern electromagnetic actuator design are introduced. Subsequently, two magnet design tools are developed based on these theories. One is magnetic surface charge model for 3D magnetic field modeling replacing 3D finite element model; another is Fourier series analytical model in 2D dimensions, which focus on harmonics of magnet array. Force and torque model of single magnet array based on Lorenz force law is introduced in section 2.4, which is used to evaluate M-Magnet array design in chapter 3.

2.1 Maxwell Equations [21]

Maxwell equations are the principles behind planar motion design. There are a set of four equations, with the status of physical laws, stating the relationship between the electric and magnetic fields and their sources being charge density and current density. Maxwell equations can be written either in the integral or differential form. The integral form is easier for explaining the meaning of electromagnetic field, whereas the differential form is better suited for mathematical modelling.

- Gauss's law for electric field:

$$\oint_S \varepsilon_0 \vec{E} \cdot d\vec{a} = \int_V \rho dv \qquad (2.1)$$

$$\nabla \cdot \varepsilon_0 \vec{E} = \rho \qquad (2.2)$$

This is the first law to state that the surface-integral of the displacement flux density ($\epsilon_0\vec{E}$) over any closed three dimensional surface S, for instance a sphere, equals to the charge enclosed within the closed surface. Where $\epsilon_0 = 8.854 \times 10^{-12} F/m$ is the permittivity in free space, and ρ is the charge density. With electromagnetism this law is not used, because in electromagnetic actuators all electrical charges are bound, which means that they are not free and always in equilibrium with the positive charge of protons of the wires that are used to carry the current.

- Gauss's law for magnetic field (Magnetic Flux Continuity):

$$\int_S \mu_0 \vec{H} \cdot d\vec{a} = 0 \qquad (2.3)$$

$$\nabla \cdot \mu_0 \vec{H} = 0 \qquad (2.4)$$

The second law of Gauss states that the surface-integral of the magnetic field over a closed surface S is always zero. Where $\mu_0 = 4\pi \times 10^{-7} H/m$ is the permeability of free space, and $\vec{H}$ is magnetic field strength. With any closed surface, the magnetic flux entering the volume within the closed surface is equal to the magnetic flux that exits that volume. Gauss's law on magnetic fields is based on the observation that magnets always act as dipoles, north and south poles where the flux flows internally from south pole to north pole and externally back from north pole to south pole.

- Faraday's law:

$$\oint_C \vec{E} \cdot d\vec{s} = -\frac{d}{dt} \int_S \mu_0 \vec{H} \cdot d\vec{a} \qquad (2.5)$$

$$\nabla \times \vec{E} = -\mu_0 \frac{\partial \vec{H}}{\partial t} \qquad (2.6)$$

The third Maxwell equation gives the relation between a change in the magnetic field and the resulting induced electrical potential difference in a wire that surrounds that field. This law states

that the line-integral of the electrical field over a contour C equals to the change of the flux through the open surface S bounded by the contour C. The minus sign indicates that the direction of the electric field is opposite to the vector $d\vec{s}$, which explains several properties of electromagnetic actuators, for instance damping effect when manually dragging magnets over stator coils.

- Ampere's law:

$$\oint_C \vec{H} \cdot d\vec{s} = \int_S \vec{J} \cdot d\vec{a} + \frac{d}{dt} \int_S \varepsilon_0 \vec{E} \cdot d\vec{a} \qquad (2.7)$$

$$\nabla \times \vec{H} = \vec{J} + \varepsilon_0 \frac{\partial \vec{E}}{\partial t} \qquad (2.8)$$

The fourth Maxwell equation gives the principle of the creation of a magnetic field by an electric current, where $\vec{J}$ is the current density. This law states that the line-integral of the magnetic field over a contour C is equal to the sum of two terms. The first term represents the current that flows through the opening of the contour and the second term represents the change of the electric field over the surface that is enclosed by the contour. The second term is in reality not relevant for electromagnetic actuators, again due to the bound character of the charges as mentioned with Gauss's law on electric field.

2.2 3D Magnetic Surface Charge Model (3DMM)

Although the first Maxwell equations in (2.1) and (2.2) are not used in electromagnetism because all electrical charges are bound in electromagnetic actuator, these equations can be used to build magnetic field model as analogous analysis. The source of an electroquasistatic (EQS) field is a scalar [21], the charge density ρ of (2

.2). In free space, the source of a magnetoquasistatic (MQS) field is a vector, the current density $\vec{J}$ in (2.8) without displacement current density $\varepsilon_0 \frac{\partial \vec{E}}{\partial t}$. Scalar sources are simpler than vector sources and this is the motivation that using Gauss's law on electric field to do equivalent analysis of magnetic field.

2.2.1 Surface Charge Potential in Electric Field [21]

According to Faraday's law (2.6) in electroquasistatic field, electric field intensity can be written by

$$\vec{E} = -\nabla\Phi \qquad (2.9)$$

where Φ is the potential of electric field. Further, the electric field potential can be derived by solving Poisson's equation based on Gauss's law of (2.2).

$$\Phi(\vec{r}) = \int_{V'} \frac{\rho_s(\vec{r'})dv'}{4\pi\varepsilon_0 \left|\vec{r} - \vec{r'}\right|} \qquad (2.10)$$

where $\vec{r}$ is the vector of observer at which the potential is evaluated, $\vec{r'}$ is the vector of source. If the charge density is confined to regions that can be described by surfaces having a very small thickness compared to the distance between observation point and the surface where charge is distributed, then electric field potential of volume in (2.10) can be expressed as surface charge potential:

$$\Phi(\vec{r}) = \int_{A'} \frac{\sigma_s(\vec{r'})da'}{4\pi\varepsilon_0 \left|\vec{r} - \vec{r'}\right|} \qquad (2.11)$$

where σ_s is the surface charge density.

2.2.2 Analogous Analysis of Magnetic Field [21]

When the observation point is far away from a small current loop, this loop can be viewed as if it were a "magnetic" dipole, considering of two equal and opposite magnetic charges $\pm q_m$ spaced a distance d apart. The magnetic charges (monopoles) are source of divergence of the magnetic flux density $\mu_0\vec{H}$, analogous to electric charges as source of divergence of the displacement flux density $\varepsilon_0\vec{E}$. Thus, it's convenient to introduce magnetic charge so that the field produced by a small current loop can be pictured as the field of a magnetic dipole. Then, equations of (2.9), (2.10) and (2.11) in above section can be applied to magnetic charge in analogous equations:

$$\overrightarrow{H} = -\nabla\Psi \qquad (2.12)$$

$$\Psi(\vec{r}) = \int_{V'} \frac{\rho_m(\overrightarrow{r'})dv'}{4\pi\mu_0\left|\vec{r} - \overrightarrow{r'}\right|} \qquad (2.13)$$

$$\Psi(\vec{r}) = \int_{S'} \frac{\sigma_m(\overrightarrow{r'})da'}{4\pi\mu_0\left|\vec{r} - \overrightarrow{r'}\right|} \qquad (2.14)$$

where Ψ is magnetic field potential, $\rho_m$is magnetic charge density, and $\sigma_m$is magnetic surface charge density. However, magnetic field approximation by small current loop is different from the field by magnetic charge dipole in (2.4). Inside the source region, approximation field has $\nabla \cdot \mu_0\vec{H} \neq 0$, and real magnet has solenoidal H field. But the magnetic field of interest in planar motor is not inside the source region, typically, at least 1mm away. Hence, we can tolerate this difference.

2.2.3 3D Analytical Model of Magnet

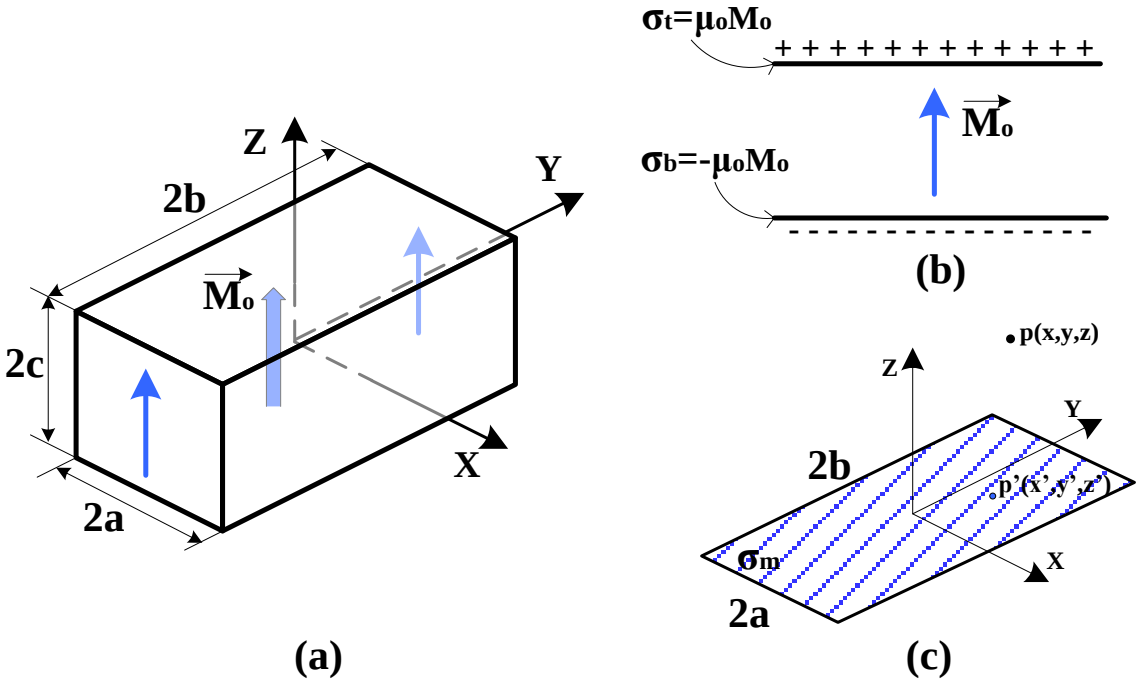

Figure 2-1 Single rectangular single permanent magnet (a) Definition of the variables of magnet (b) Magnetic surface charge model; (c) Single layer surface charge model

There is a single rectangular prism permanent magnet with coordinate system (x, y, z) centered inside the body. The lengths of the magnet in x, y and z-directions are 2a, 2b and 2c respectively, as shown in figure 2-1a. The magnet is magnetized in +z direction and uniformly distributed in x and y-axis. The magnetization of magnet can be expressed as $\vec{M} = M_0\vec{k}$, where $M_0 = {B_r}/{\mu_0}$, and

B_r is the magnet remanence. With the assumption that the relative permeability is equal to 1 in and outside the permanent magnet, which is reasonable because relative permeability of permanent magnet is around 1.01-1.05, the magnetic surface charge, σ_m, is equal to the B_r at top surface and $-B_r$ at bottom surface respectively [22], which is depicted in figure 2-1b. According to Gauss's law on electric field in (2.1), in analogy, its magnet form is

$$\nabla \cdot \mu_0 \overrightarrow{M} = \rho_m \qquad (2.15)$$

thus, the magnetic charge inside the magnet is zero because divergence of uniform magnetization inside the magnet is zero.

Substituting (2.14) into (2.12) and take the gradient of magnetic potential relative to observation coordinates $\vec{r}$, the relation between magnetic field strength and magnetic charge is formulated as

$$H(\vec{r}) = \int_{S'} \frac{\sigma_m(\overrightarrow{r'})(\vec{r} - \overrightarrow{r'})da'}{4\pi\mu_0 \left|\vec{r} - \overrightarrow{r'}\right|^3} \qquad (2.16)$$

with $B = \mu_0 H$, magnetic flux density is obtained. If we look at a single layer of magnetic surface charge with coordinates in the rectangular center and lengths 2a and 2b in x and y-axis respectively, as shown in figure 2-1c, any observation point $p(x, y, z)$ is undergoing a three-dimensional magnetic field(B_x, B_y, B_z) [23]:

$$B_x^s = \frac{\sigma_m}{4\pi} \sum_{i=0}^{1} \sum_{j=0}^{1} (-1)^{i+j} \ln(R - T) \qquad (2.17)$$

$$B_y^s = \frac{\sigma_m}{4\pi} \sum_{i=0}^{1} \sum_{j=0}^{1} (-1)^{i+j} \ln(R - S) \qquad (2.18)$$

$$B_z^s = \frac{\sigma_m}{4\pi} \sum_{i=0}^{1} \sum_{j=0}^{1} (-1)^{i+j} a \tan 2\left(\frac{ST}{Rz}\right) \qquad (2.19)$$

where $S = x - (-1)^i a$, $T = y - (-1)^i b$, $R = \sqrt{S^2 + T^2 + z^2}$. The derivation of above equations is attached in Appendix B.

By superposition principle, magnetic field flux density at any given point $p(x, y, z)$ in figure 2-1a is given by,

$$B_n = B_n^t + B_n^b \quad (2.20)$$

where n represents x, y, or z, t represents top surface of magnet, and b represents bottom surface of magnet. By plugging top surface charge density, $\sigma_m^t = \mu_0 M_0$, and bottom surface charge density, $\sigma_m^b = -\mu_0 M_0$, into equation (2.17), (2.18), (2.19) and (2.20), 3D surface charge model of single rectangular prism magnet is obtained, which is described by following equations [24]:

$$B_x = \frac{B_r}{4\pi}\sum_{i=0}^{1}\sum_{j=0}^{1}\sum_{k=0}^{1}(-1)^{i+j+k}\ln(R-T) \quad (2.21)$$

$$B_y = \frac{B_r}{4\pi}\sum_{i=0}^{1}\sum_{j=0}^{1}\sum_{k=0}^{1}(-1)^{i+j+k}\ln(R-S) \quad (2.22)$$

$$B_z = \frac{B_r}{4\pi}\sum_{i=0}^{1}\sum_{j=0}^{1}\sum_{k=0}^{1}(-1)^{i+j+k}a\tan 2(\frac{ST}{RU}) \quad (2.23)$$

where $U = z - (-1)^k c$, $R = \sqrt{S^2 + T^2 + U^2}$, S and T are same as (2.19).

In sum, although surface charge model of magnet is approximation of magnet dipole in (2.2), it's good enough to simulate magnet field outside of magnet, which is the field of interest in planar motor design. Further, the computation of this model is much fast compared to finite element model simulation.

2.3 2D Fourier series Analytical Model (2DFM)

From magnetic field harmonic point of view, 3D magnetic surface charge model is still too complex to apply to planar motor analysis because too many details about the magnetic field, for instance fringing effect of magnet can be simulated by 3D analytical model. If we only take 3D analytical model of a single Halbach array, four magnet blocks per period, into account, then harmonics of magnetic field will be coupled with frequencies from magnet edge. At this point,

2D analytical model based on Fourier series is much better than 3D analytical model because it focus on real harmonic components of Halbach array.

2.3.1 Vector Potential of Magnetic Field

According to Gauss's law (2.4) and Ampere's law (2.8), magnetic field can be simplified as:

$$\begin{aligned} \nabla \times \vec{H} &= \vec{J} \\ \nabla \cdot \mu_0 \vec{H} &= 0 \end{aligned} \qquad (2.24)$$

in MQS systems [21]. Here magnetic field has a vector source, current density $\vec{J}$, instead of scalar source in (2.12). Then a vector potential $\vec{A}$ instead of scalar potential $\vec{\Psi}$ is used to describe magnetic field.

$$\mu_0 \vec{H} = \nabla \times \vec{A} \qquad (2.25)$$

Again, in MQS systems, it's convenient to select a solenoidal vector potential or set the Coulomb gauge.

$$\nabla \cdot \vec{A} = 0 \qquad (2.26)$$

Substituting (2.25) into (2.24), and using vector identity $\nabla \times \left(\nabla \times \vec{A}\right) = \nabla\left(\nabla \cdot \vec{A}\right) - \nabla^2 \vec{A}$, we have vector Poisson's equation of magnetic field.

$$\nabla^2 \vec{A} = -\mu_0 \vec{J} \qquad (2.27)$$

Generally, when a magnet body is immersed in an applied magnetic field, the H-field, during magnetization, the magnetic flux density at any point is given by

$$\vec{B}_{total} = \vec{B}_{applied} + \vec{B}_{induced} \qquad (2.28)$$

where $\vec{B}_{applied} = \mu_0 \vec{H}_f$ is magnetic flux density in free space, and $\vec{B}_{induced} = \mu_0 \vec{M}$ is induced magnetic flux density by the applied field. After magnetization, there is no free space H-field,

thus only induced field remains for permanent magnet. Plugging $\vec{B}_{induced} = \mu_0 \vec{M} = \mu_0 \vec{H}_{induced}$ into (2.24), equivalent current density can be achieved by

$$\nabla \times \vec{M} = \vec{J} \qquad (2.29)$$

Combining (2.27) and (2.29), we have the relationship between vector potential $\vec{A}$ and magnetization $\vec{M}$.

$$\nabla^2 \vec{A} = -\mu_0 (\nabla \times \vec{M}) \qquad (2.30)$$

2.3.2 Magnet Model Based on Fourier series

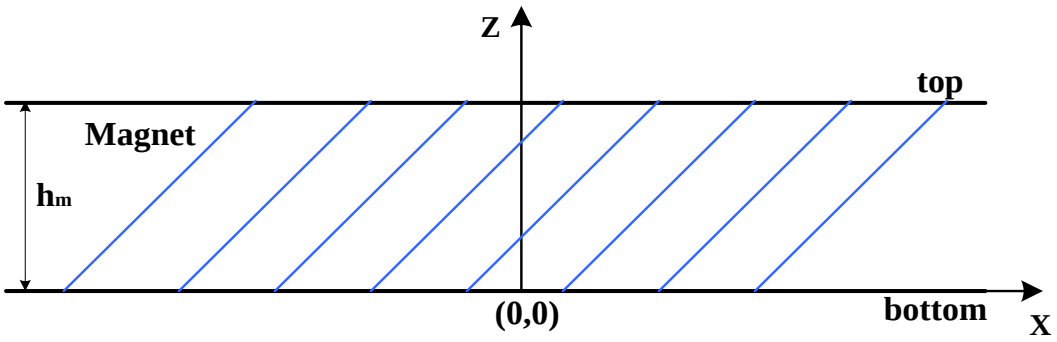

Figure 2-2 Ideal magnet with finite height in z and infinite length in x

For 2D analysis of magnet field in figure 2-2, magnetization $\vec{M}$ in Cartesian coordinates is written by

$$\vec{M} = M_x \vec{i} + M_z \vec{k} \qquad (2.31)$$

Correspondingly, the vector potential $\vec{A}$ has only a y-directed component $\vec{A} = A_y \vec{j}$. Thus the vector Poisson equation (2.30) reduces to a scalar equation

$$\left(\frac{\partial^2}{\partial^2 x} + \frac{\partial^2}{\partial^2 z}\right) A_y = \mu_0 \left(-\frac{\partial M_x}{\partial z} + \frac{\partial M_z}{\partial x}\right) \qquad (2.32)$$

The magnetization distribution M_x and M_z can be written as a sum of Fourier series [25][26] as described by

$$M_x = \sum_{i=1} M_{xn}, M_z = \sum_{i=1} M_{zn} \quad (2.33)$$

$$M_{xn} = \frac{1}{2\lambda}\int_0^{\lambda} M_x e^{j\frac{x}{\lambda_n}} dx \quad (2.34)$$

$$M_{zn} = \frac{1}{2\lambda}\int_0^{\lambda} M_z e^{j\frac{x}{\lambda_n}} dx \quad (2.35)$$

where λ is fundamental spatial period of magnet array, and $\lambda_n = \frac{\lambda}{2\pi n}, n = 1,2,3 \ldots \infty$ is spatial period of specific harmonic. Substituting (2.34) and (2.35) into (2.32), and solving Poisson equation by superposition of particular and homogeneous solutions [26] with boundary conditions that potentials are continued at the boundary and go to zero at infinity, potentials in Fourier series at top surface and bottom surface of figure 2-2 are achieved. Then applying potential to (2.25) with $\vec{B} = \mu_0 \vec{H}$, magnetic flux density in Fourier series on top surface and bottom surface of magnet are written as

$$\begin{cases} B_{xn}^t = (-\frac{\mu_0}{2} M_{xn} + j\frac{\mu_0}{2} M_{zn}) \cdot (1 - e^{-\frac{h_m}{\lambda_n}}) \\ B_{zn}^t = (j\frac{\mu_0}{2} M_{xn} + \frac{\mu_0}{2} M_{zn}) \cdot (1 - e^{-\frac{h_m}{\lambda_n}}) \end{cases} \quad (2.36)$$

$$\begin{cases} B_{xn}^b = (-\frac{\mu_0}{2} M_{xn} - j\frac{\mu_0}{2} M_{zn}) \cdot (1 - e^{-\frac{h_m}{\lambda_n}}) \\ B_{zn}^b = (-j\frac{\mu_0}{2} M_{xn} + \frac{\mu_0}{2} M_{zn}) \cdot (1 - e^{-\frac{h_m}{\lambda_n}}) \end{cases} \quad (2.37)$$

2.3.3 Halbach Array

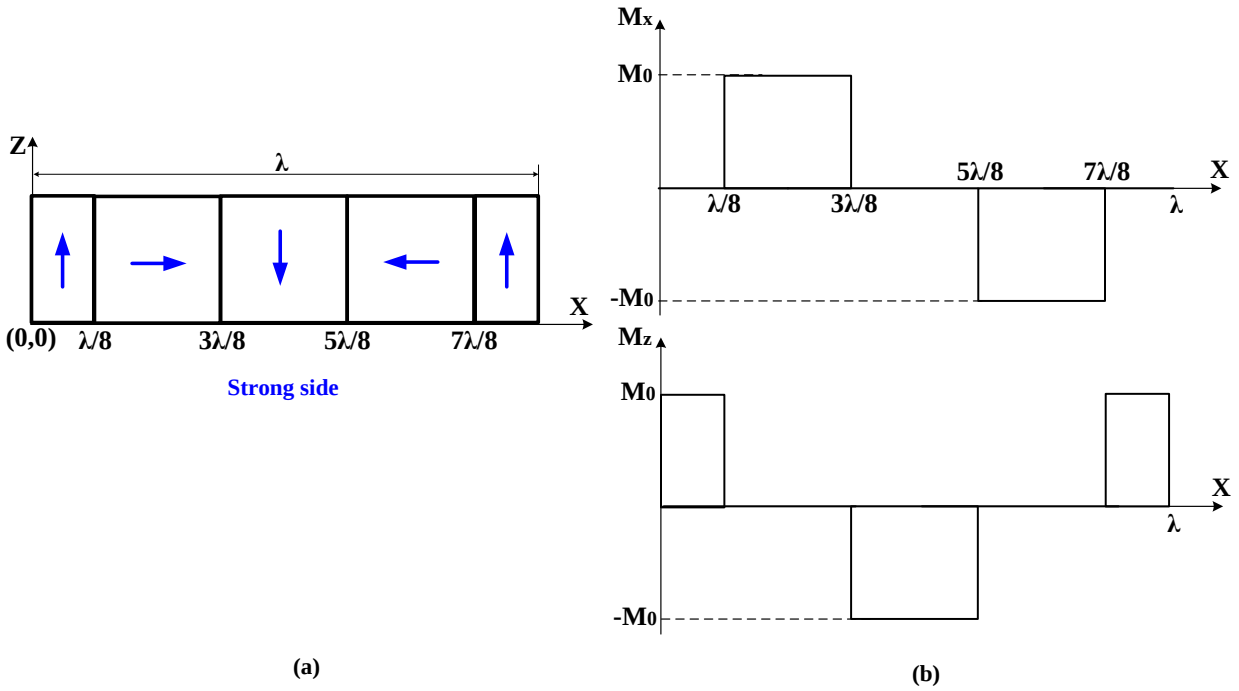

Figure 2-3 (a) Conventional Halbach array with mirror-symmetric field; (b) Magnetization components in x and z-axis

If we look at the conventional Halbach array in figure 1-9 with five blocks per period to make a mirror-symmetric field about middle vertical axis shown in figure 2-3a, magnetization components in x and z-axis are plotted in figure 2-3b. Plugging magnetization components M_x and M_z into (2.34) and (2.35) respectively, it follows that

$$M_{zn} = \frac{M_0}{2\pi n}(\sin\frac{\pi n}{4} + \sin\frac{3\pi n}{4}) = \begin{cases} \frac{\sqrt{2}M_0}{\pi n}, n = 8m+1, or, n = 8m+3 \\ -\frac{\sqrt{2}M_0}{\pi n}, n = 8m+5, or, n = 8m+7, m = 0,1,2...\infty \\ 0, n = even \end{cases} \quad (2.38)$$

$$M_{xn} = j\frac{M_0}{2\pi n}(\cos\frac{\pi n}{4} - \cos\frac{3\pi n}{4}) = j^n M_{zn} \quad (2.39)$$

Substituting (2.38) and (2.39) into (2.37), magnitude of magnetic flux density of each harmonic on bottom surface of magnet is achieved as

$$B_{xn}^{b}=\begin{cases}-j\dfrac{\sqrt{2}\mu_0 M_0}{\pi n}(1-e^{-\frac{h_m}{\lambda_n}}), n=8m+1\\ j\dfrac{\sqrt{2}\mu_0 M_0}{\pi n}(1-e^{-\frac{h_m}{\lambda_n}}), n=8m+5\ \ , m=0,1,2...\infty\\ 0, n=other\end{cases} \quad (2.40)$$

$$B_{zn}^{b}=\begin{cases}\dfrac{\sqrt{2}\mu_0 M_0}{\pi n}(1-e^{-\frac{h_m}{\lambda_n}}), n=8m+1\\ -\dfrac{\sqrt{2}\mu_0 M_0}{\pi n}(1-e^{-\frac{h_m}{\lambda_n}}), n=8m+5, m=0,1,2...\infty\\ 0, n=other\end{cases} \quad (2.41)$$

After taking Fourier inverse transform, magnetic flux density on bottom surface of conventional Halbach array is written as

$$B_x^b=\sum_{-\infty}^{\infty}B_{xn}^{b}e^{-j\frac{x}{\lambda_n}}=\frac{\mu_0}{2}[\sum_{n=1}^{\infty}(j^n+j)M_{zn}e^{j\frac{x}{\lambda_n}}-\sum_{n=1}^{\infty}(j^n+j)M_{zn}e^{-j\frac{x}{\lambda_n}}](1-e^{-\frac{h_m}{\lambda_n}}) \quad (2.42)$$

$$B_z^b=\sum_{-\infty}^{\infty}B_{zn}^{b}e^{-j\frac{x}{\lambda_n}}=\frac{\mu_0}{2}[\sum_{n=1}^{\infty}(1+j^{1-n})M_{zn}e^{j\frac{x}{\lambda_n}}+\sum_{n=1}^{\infty}(1-j^{1+n})M_{zn}e^{-j\frac{x}{\lambda_n}}](1-e^{-\frac{h_m}{\lambda_n}}) \quad (2.43)$$

From [26] the magnetic field decays exponentially in z from the source of magnet in free space for the Cartesian geometry, therefore, at any point on the strong side of magnet, the magnetic flux density is given by

$$B_x^s=\frac{\mu_0}{2}[\sum_{n=1}^{\infty}(j^n+j)M_{zn}e^{j\frac{x}{\lambda_n}}-\sum_{n=1}^{\infty}(j^n+j)M_{zn}e^{-j\frac{x}{\lambda_n}}](1-e^{-\frac{h_m}{\lambda_n}})e^{-\frac{|z|}{\lambda_n}} \quad (2.44)$$

$$B_z^s = \frac{\mu_0}{2}[\sum_{n=1}^{\infty}(1+j^{1-n})M_{zn}e^{j\frac{x}{\lambda_n}} + \sum_{n=1}^{\infty}(1-j^{1+n})M_{zn}e^{-j\frac{x}{\lambda_n}}](1-e^{-\frac{h_m}{\lambda_n}})e^{-\frac{|z|}{\lambda_n}} \quad (2.45)$$

2.4 Force and Torque Models

Planar motor is a kind of actuator based on Lorenz force law, which inherently has low mechanical stiffness between stator coils and moving magnets, and also linear relationship between current and force. To be comparable with previous work in [12], force and torque model of magnet array is analyzed by using elongated coil pattern with width w_c and thickness t_c, as shown in figure 2-4, in which a single magnet array, with width λ, height h_m and length L_m respectively, flying over the stator coils. Coordinate system (x, y, z) is centered on the bottom surface of the magnet array, and the center of gravity (CG) is coincident with the center of magnetic array. To simplify analysis, only single layer of coils is taken into account.

Lorenz force of magnetic field system in continuum representation [27] is given by

$$\vec{F} = \overrightarrow{J_f} \times \vec{B} \quad (2.46)$$

where $\vec{F}$ is force density, and $\overrightarrow{J_f}$ is current density of stator coils. Thus for specific coil with volume V, Lorenz force can also be written as [28]:

$$\vec{F} = \iiint_V \overrightarrow{J_f} \times \vec{B} dv \quad (2.47)$$

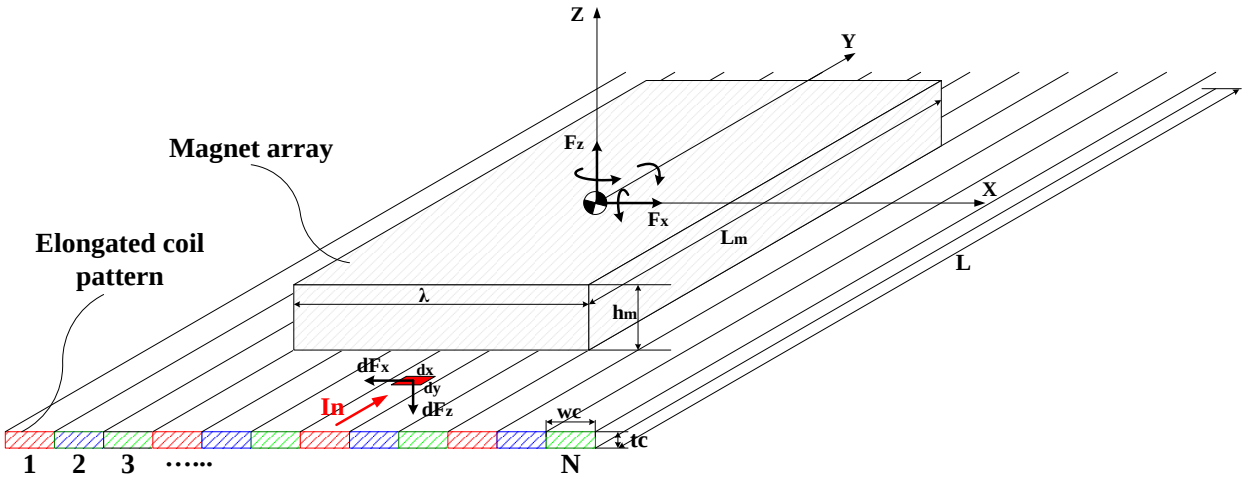

Figure 2-4 Force and torque model of single magnet array

If we look at a small region of one single coil with current I_n going through, dx and dy in width and length respectively, Lorenz force exerting on this small region due to magnetic field of the single magnet array can be written by

$$dF_x = -\frac{I_n}{w_c t_c} B_z(x,y,z)(dxdyt_c) = -\frac{I_n}{w_c} B_z(x,y,z)(dxdy) \quad (2.48)$$

$$dF_z = -\frac{I_n}{w_c t_c} B_x(x,y,z)(dxdyt_c) = -\frac{I_n}{w_c} B_x(x,y,z)(dxdy) \quad (2.49)$$

where minus sign means counter acting force on stator coils, coordinate (x, y, z) is the position of the small coil region, and I_n is uniformly distributed inside each coil. Accordingly, torques exerting on magnet array CG by this small coil region can be derived as

$$dT_x = -dF_z y = \frac{I_n}{w_c} y B_x(x,y,z)(dxdy) \quad (2.50)$$

$$dT_y = dF_z x - dF_x (z - \frac{h_m}{2}) = \frac{I_n}{w_c}(-xB_x(x,y,z) + (z - \frac{h_m}{2})B_z(x,y,z))(dxdy) \quad (2.51)$$

$$dT_z = dF_x \cdot y = -\frac{I_n}{w_c} y B_z(x,y,z)(dxdy) \quad (2.52)$$

By superposition principle, the net forces and torques exerting on CG of single magnet array are given by

$$F_x = \sum_{n=1}^{N} \int_0^L \int_0^{w_c} \frac{I_n}{w_c} \times B_z(x, y, z) dx dy \quad (2.53)$$

$$F_z = \sum_{n=1}^{N} \int_0^L \int_0^{w_c} \frac{I_n}{w_c} \times B_x(x, y, z) dx dy \quad (2.54)$$

$$T_x = \sum_{n=1}^{N} \int_0^L \int_0^{w_c} \frac{I_n}{w_c} y B_x(x, y, z) dx dy \quad (2.55)$$

$$T_y = \sum_{n=1}^{N} \int_0^L \int_0^{w_c} \frac{I_n}{w_c} [-x B_x(x, y, z) + (z - \frac{h_m}{2}) B_z(x, y, z)] dx dy \quad (2.56)$$

$$T_z = \sum_{n=1}^{N} \int_0^L \int_0^{w_c} -\frac{I_n}{w_c} y B_z(x, y, z) dx dy \quad (2.57)$$

where L is the length of elongated current coil, w_c is the width of a single coil, which is equal to $\frac{\lambda}{6}$, and N is the number of coils underneath magnet array.

Chapter 3: Novel M-Magnet Array Design for Planar Motor

In this chapter, a novel M-Magnet array is presented in several aspects: magnetic field and geometry design, array layout for 2D actuation and 6D actuation, manufacturing tolerance analysis and array assembly design. Magnetic field analysis tools based on 3D magnetic surface charge model and 2D Fourier series model from chapter 2 are developed to analyze the magnetic field of M-Magnet array. By using 2D analytical model, high-order harmonics of M-Magnet array are achieved. Based on harmonic characteristic of M-Magnet array, a novel hybrid array is presented. Theoretically it can perfectly cancel out 5^{th} harmonic, which leads to the dominant 6^{th} force ripple in planar motor. By using 3D analytical model of M-Magnet array along with force and torque models from section 2.4, dragging and levitation forces and torques around three Cartesian axes of single array are achieved. Correspondingly 6^{th} force and torque ripples of M-Magnet array are also obtained. Furthermore, manufacturing tolerances in magnetization angle and geometric dimension of length, height and width are investigated based on 3D analytical model and numerical integration of Lorentz force. Finally, array assembly tool and procedure are discussed in section 3.4.

3.1 M-Magnet Array

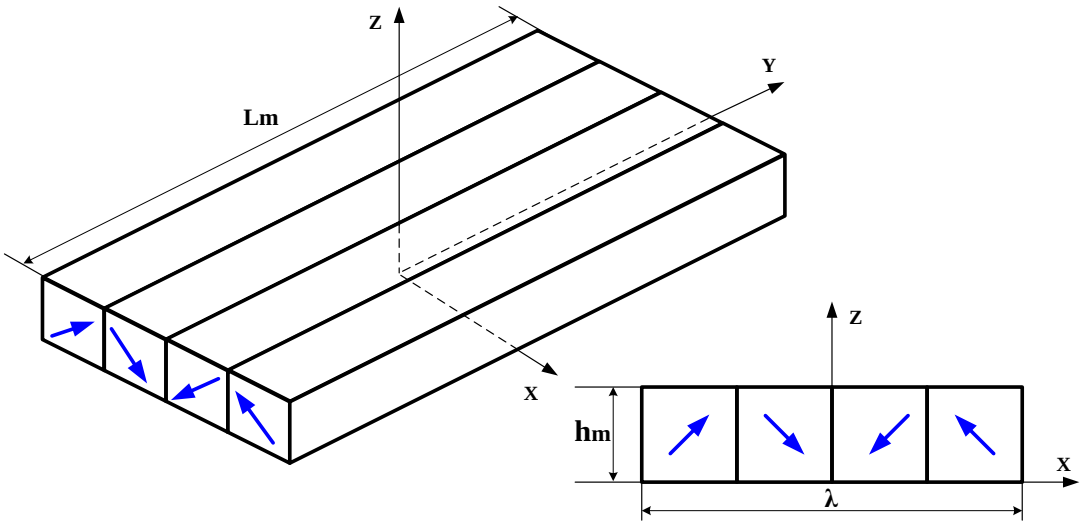

Figure 3-1 M shape magnet array

Figure 3-1 shows the M shape magnet array, which consists of four magnet pieces. Each piece is identical with a magnetization axis along 45 degree direction, and magnetization is uniformly distributed in y-axis. By rotating 90 degree along clockwise direction from left to right in each subsequent block, magnetization axes of four blocks generate an "M" shape pattern.

An M-Magnet array has only four identical magnets per spatial period to create mirror-symmetric magnetic field about middle axis (z). This is different from other Halbach arrays being designed in [17][25][29][30][31]. For these conventional Halbach array designs, there are either 5 pieces or 9 pieces to generate mirror-symmetric magnetic field. This section will go through all of characteristics of M-Magnet.

3.1.1 Array Geometric and Material Parameters

Based on previous work in [12] and [17], the optimization cost function for magnet array design is to maximize acceleration that mover can achieve when current density is given.

- M-Magnet Array Geometry

According to the 2D analytical model in (2.44) and (2.45), and force model in (2.53) and (2.54), if we only look at the fundamental component of Halbach array, force is proportional to $(1 - e^{-\frac{h_m}{\lambda_1}})$. For an M-Magnet array in figure 3-1, mass is given by $\rho_{magnet} h_m L_m \lambda$, thus based on Newton's law, acceleration is proportional to $\frac{1}{h_m}(1 - e^{-\frac{h_m}{\lambda_1}})$. Combining them together to maximize both, we have the cost function given by

$$f(h_m) = \frac{1}{h_m}(1 - e^{-\frac{h_m}{\lambda_1}})^2 \qquad (3.1)$$

where $\lambda_1 = \frac{\lambda}{2\pi}$ coming from fundamental component of magnetic field. From (3.1), optimal height of magnet array is obtained, which is at $h_m = \frac{\lambda}{5}$. On the other hand, An M-Magnet array has four pieces per period, the width of each magnet is $\frac{\lambda}{4}$. If we choose rectangular cross-section instead of square, we have to use four different types of magnet pieces, which will lead to high manufacturing costs and assembly complexity. For this reason, we use square cross-section magnet with $\frac{\lambda}{4}$ square side.

From [17], $\lambda = 30mm$ is chosen for the balance of cost, manufacturability and actuator performance.

- Permanent Magnet Material

In this project, VACODYM 837TP magnet material (45 MGOe) with 2-deg magnetization orientation tolerance is chosen because its operating temperature can go to $150^0 C$, which is very useful in planar motor design since fully operating magnetically levitation force of planar motor will result in high thermal radiation from stator coils for applications without forced cooling

system. Furthermore, this material has much high remanence, $B_r = 1.36[T]$ with 2% tolerance, which leads to high force density.

3.1.2 3D Field of M-Magnet Array

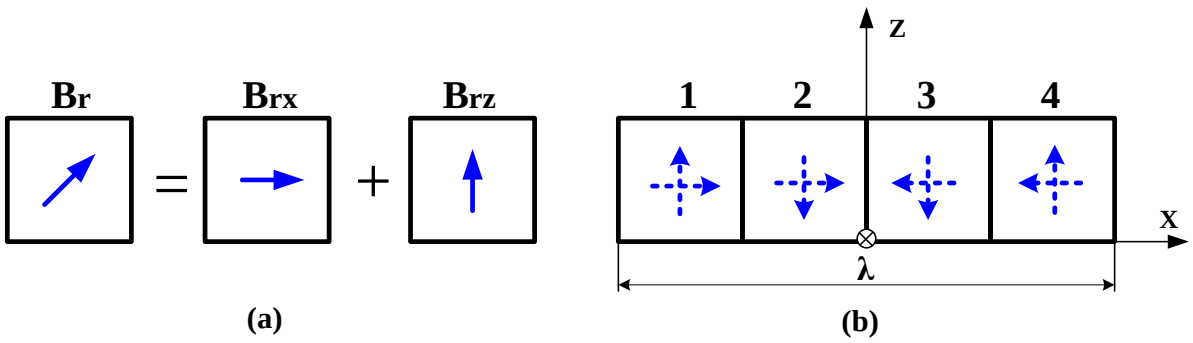

Figure 3-2 (a) Magnetic field decomposition; (b) equivalent M-Magnet array

In the Cartesian coordinate system, magnetic field magnetized in 45 degree direction can be decomposed into x and z components, keeping magnetization uniformly distribution in y-axis, as shown in figure 3-2a. Magnetic flux density of x or z component is equal to $\frac{B_r}{\sqrt{2}}$. Correspondingly, the M-Magnet array can be replaced by equivalent superposition array in figure 3-2b, where each magnet piece is superposed by its x and z components. Magnetic field of M-Magnet array can be achieved by superposition of all fields from magnetization components of each magnet block

$$\begin{aligned} B_x &= \sum_{i=1}^{4} (B_x^{xi} + B_x^{zi}) \\ B_y &= \sum_{i=1}^{4} (B_y^{xi} + B_y^{zi}) \\ B_z &= \sum_{i=1}^{4} (B_z^{xi} + B_z^{zi}) \end{aligned} \qquad (3.2)$$

where B_x^{xi} is magnetic flux density in x-axis generated by x component of magnet block i, i is magnet index shown in figure 3-2b, and B_x^{zi} is magnetic flux density in x-axis generated by z component of magnet block i, similar as magnetic flux density in y and z-axis.

For z component of 45 degree magnetization, 3D analytical model of (2.21), (2.22) and (2.23) built in section 2.2 can be applied to (3.2) directly, whereas for x component, coordinate needs to be rotated by 90 degree around y-axis before applying these equations. Furthermore, coordinate translation also needs to be taken into account for each magnet with x and z offsets between magnet center and origin of Cartesian coordinate system.

Figure 3-3 and figure 3-5 shows the magnetic field of single M-Magnet array by 3D magnetic surface charge model (3DMM), and modeling error between 3DMM and FEM from COMSOL is also calculated in figure 3-4 and figure 3-6. Roughly speaking, maximum error is less than 1.5mT, which is about 0.5% of the peak of magnetic flux density at the air gap of $\frac{\lambda}{5}$. As air gap decreases from $\frac{\lambda}{5}$ to $\frac{\lambda}{30}$, maximum modeling error increases to 10mT, which is about 1% of maximum flux density.

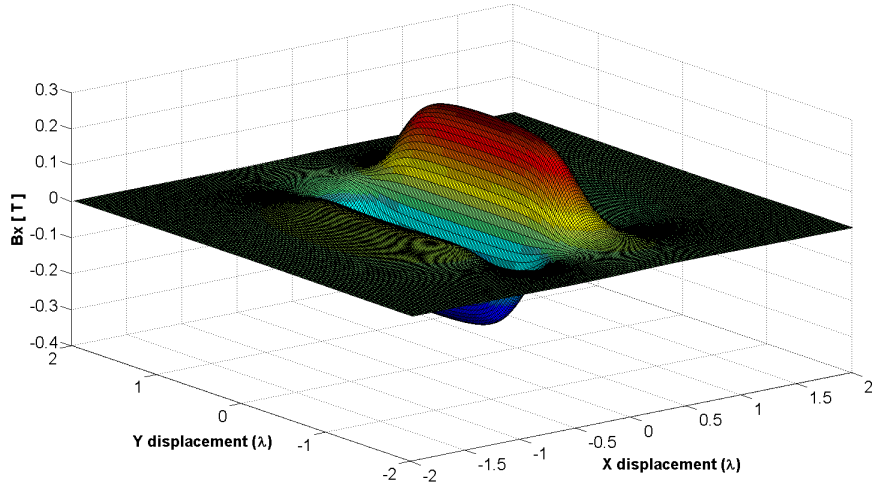

(a) Magnetic flux density in x axis at z=-λ/5

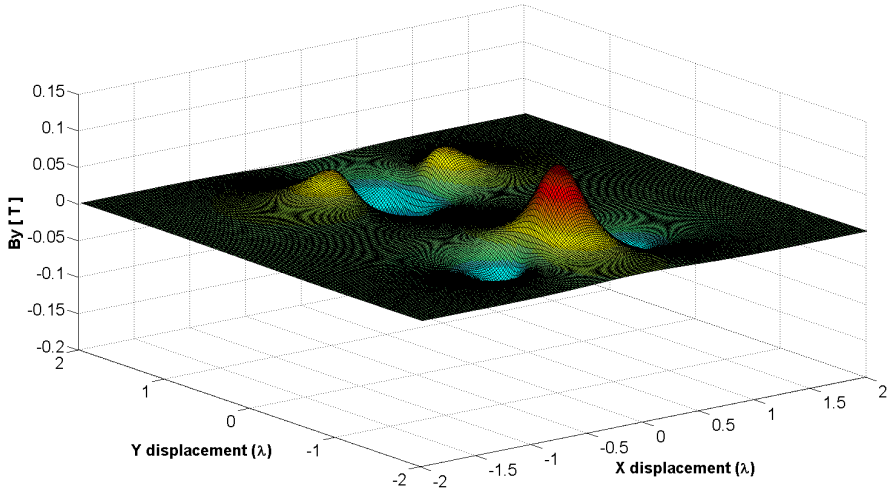

(b) Magnetic flux density in y axis at z=-λ/5

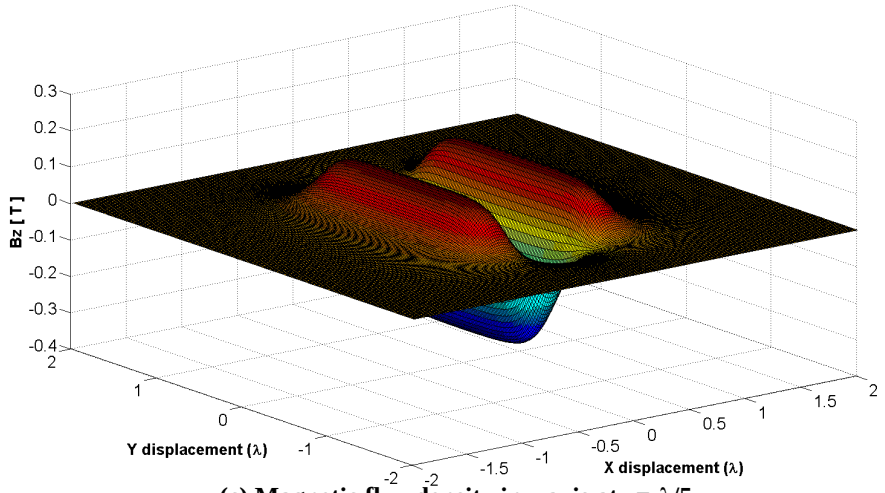

(c) Magnetic flux density in z axis at z=-λ/5

Figure 3-3 Magnetic flux density of M-Magnet array by 3D analytical model at $z = -\frac{\lambda}{5}$

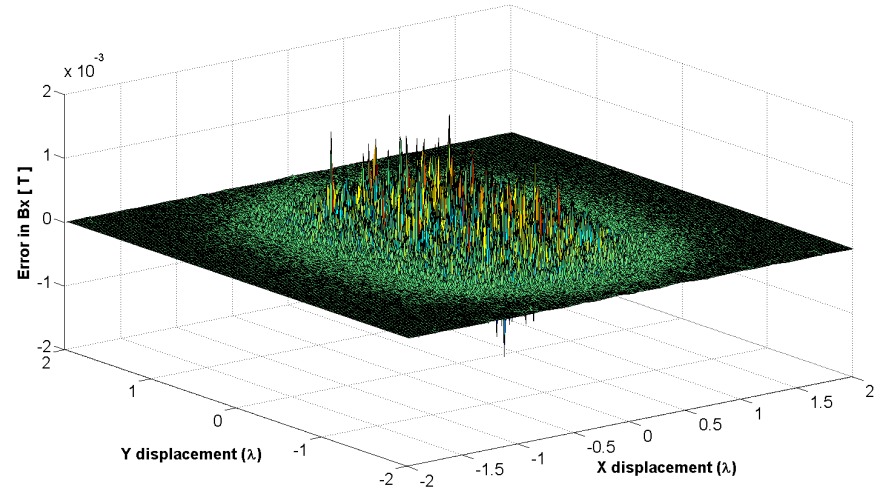

(a) Error of magnetic flux density in x axis at z=-λ/5

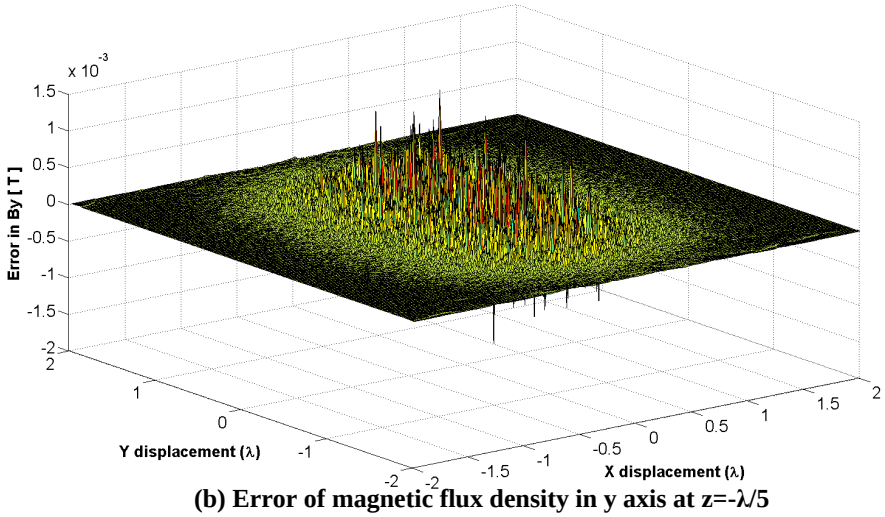

(b) Error of magnetic flux density in y axis at z=-λ/5

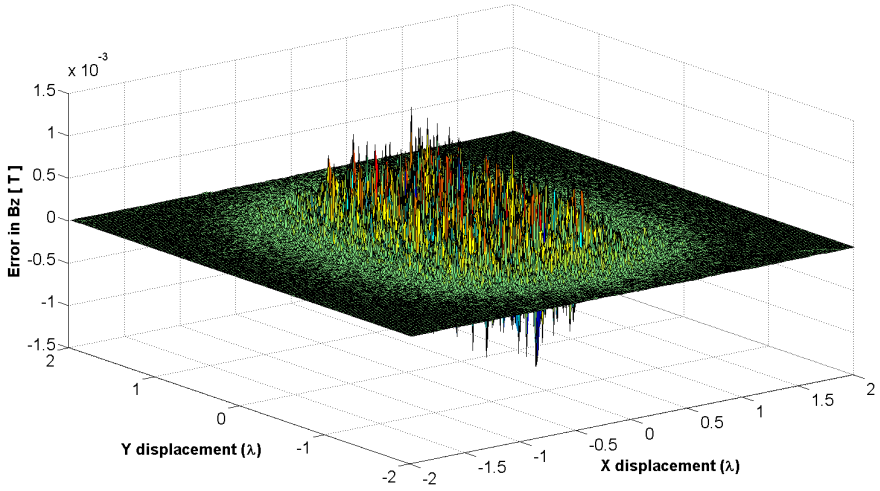

(c) Error of magnetic flux density in z axis at z=-λ/5

Figure 3-4 Field comparison between 3DMM and FEM (COMSOL) at $z = -\frac{\lambda}{5}$ ($Error = B_{3DMM} - B_{FEM}$)

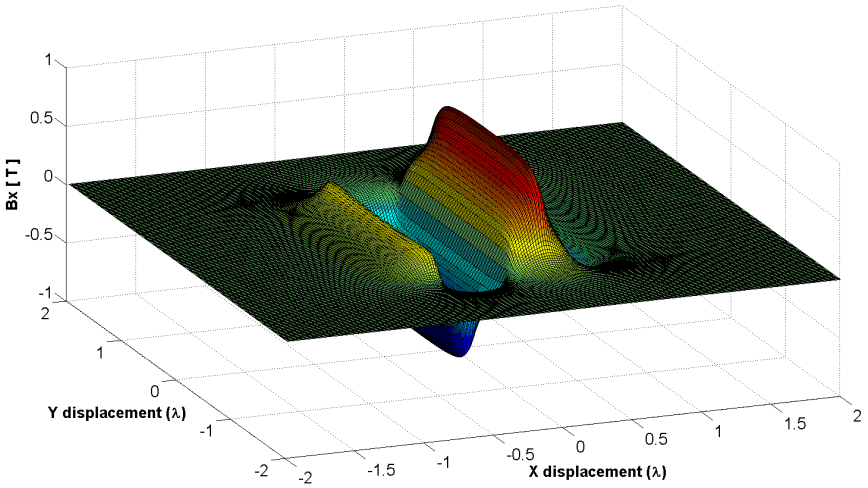

(a) Magnetic flux density in x axis at z=-λ/30

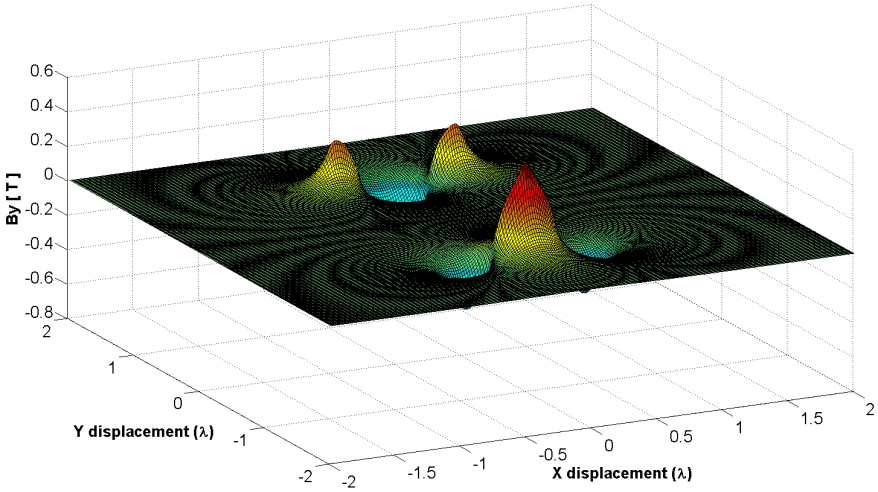

(b) Magnetic flux density in y axis at z=-λ/30

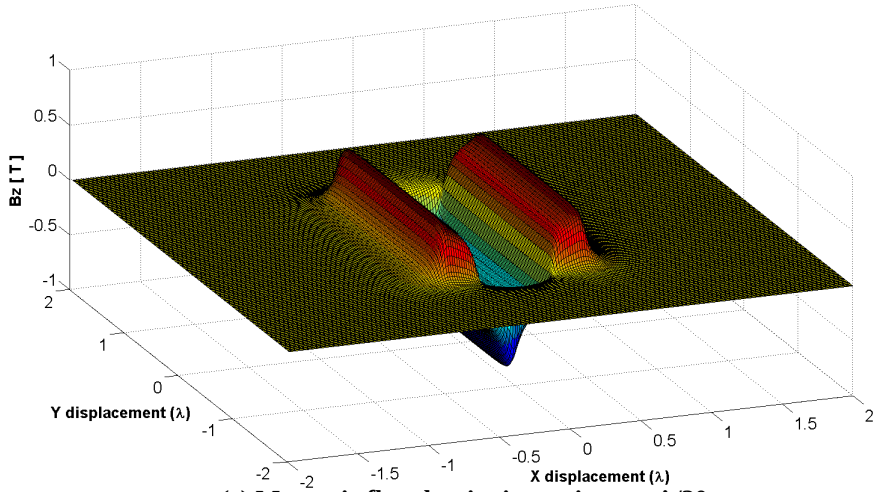

(c) Magnetic flux density in z axis at z=-λ/30

Figure 3-5 Magnetic flux density of M-Magnet array by 3D analytical model at $z = -\frac{\lambda}{30}$

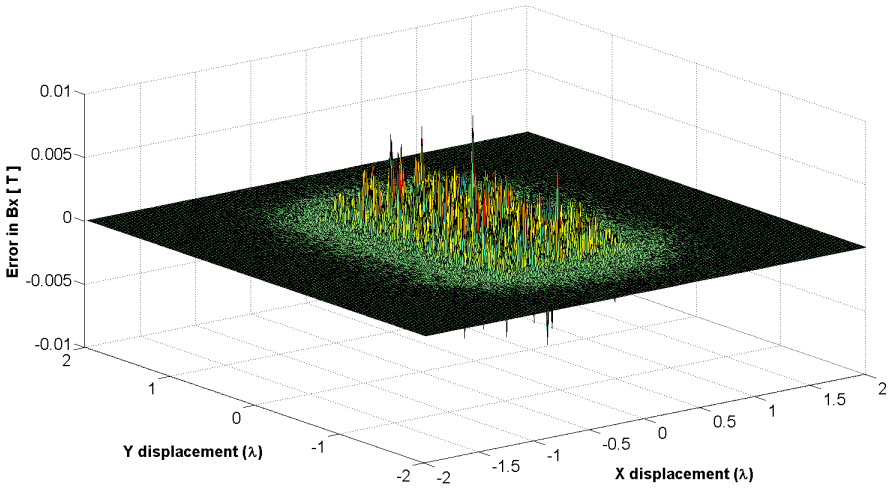

(a) Error of magnetic flux density in x axis at z=-λ/30

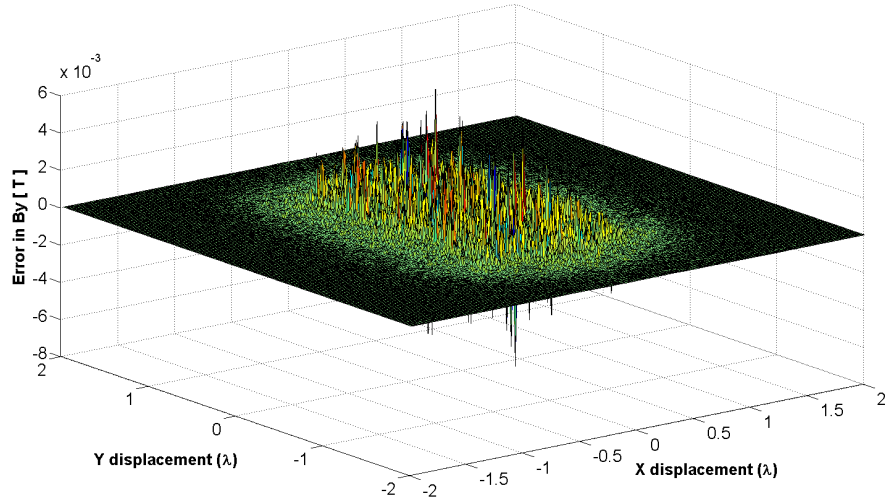

(b) Error of magnetic flux density in y axis at z=-λ/30

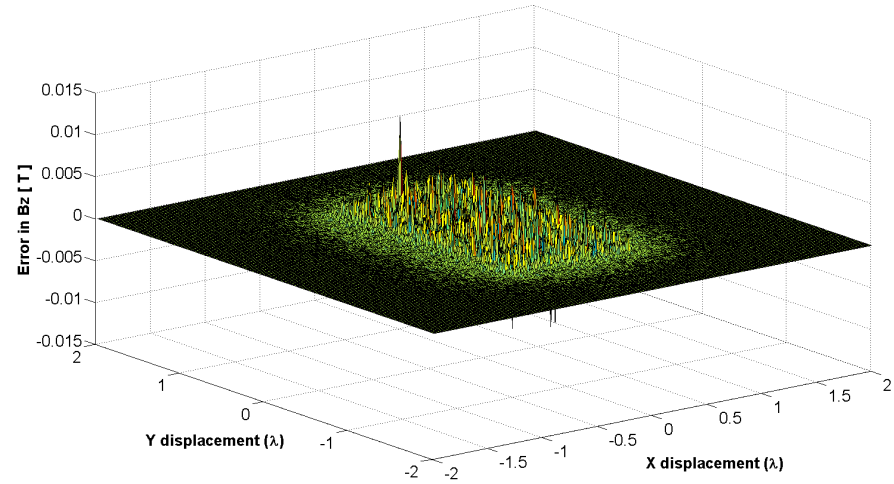

(c) Error of magnetic flux density in z axis at z=-λ/30

Figure 3-6 Field comparison between 3DMM and FEM (COMSOL) at $z = -\frac{\lambda}{30}$ ($Error = B_{3DMM} - B_{FEM}$)

3.1.3 2D Model of M-Magnet Array

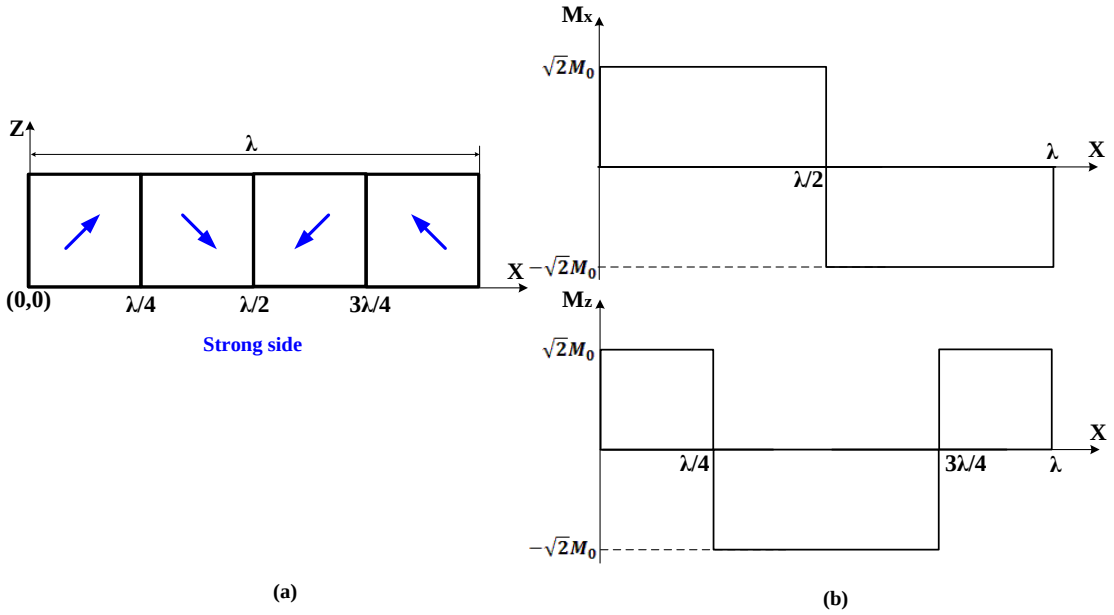

Figure 3-7 (a) M-Magnet array with mirror-symmetric field; (b) Magnetization components in x and z-axis

Similarly as figure 3-2a, we can also decompose magnetization vector of each magnet piece in M-Magnet array (figure 3-7a) into x and z components respectively, then magnetization functions in x and z-axis are obtained, as shown in figure 3-7b. Plugging these magnetization components M_x and M_z into (2.34) and (2.35), it follows that

$$M_{zn} = \frac{\sqrt{2}M_0}{\pi n}\sin\frac{\pi n}{2} = \begin{cases} \dfrac{\sqrt{2}M_0}{\pi n}, n = 4m+1 \\ -\dfrac{\sqrt{2}M_0}{\pi n}, n = 4m+3, m = 0,1,2...\infty \\ 0, n = even \end{cases} \qquad (3.3)$$

$$M_{xn} = j\frac{M_0}{2\pi n} = j^n M_{zn} \qquad (3.4)$$

Substituting (3.3) into (2.44) and (2.45) respectively, 2D analytical model of M-Magnet array based on Fourier series is achieved.

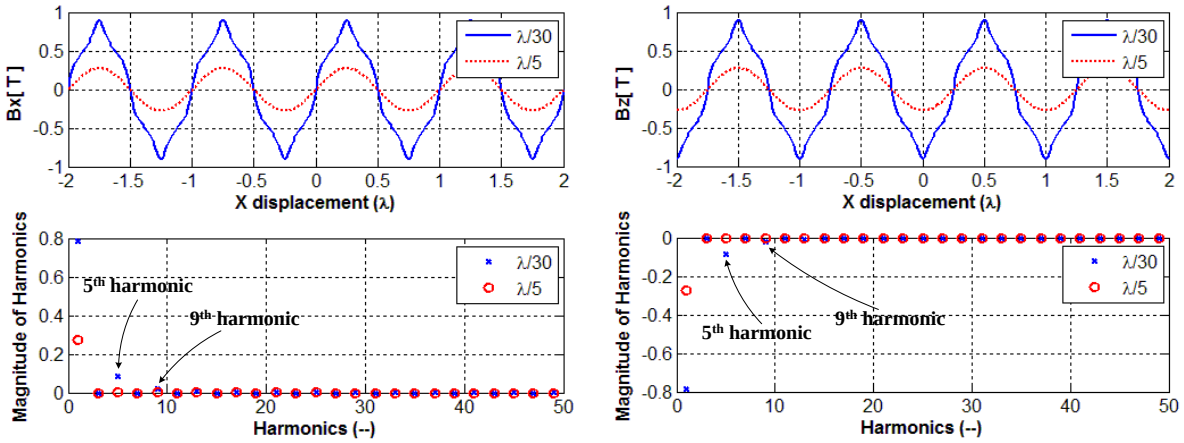

(a) (b)

Figure 3-8 Magnetic flux density of M-Magnet array by 2D analytical model (a) magnetic flux density in x-direction (Bx) (b) magnetic flux density in z-direction (Bz)

From (2.40) and (2.41), it's noticed that on the surface of Halbach array there are only magnetic field harmonics at 5^{th} ,9^{th} ,13^{th} ,17^{th} ,…, other odd and even harmonics are zero. When planar motor gap increases to $\frac{\lambda}{30}$, only 5^{th} and 9^{th} harmonics left shown in figure 3-8. At this gap, the magnitude of 5^{th} harmonic is about 10% of fundamental component and 9^{th} harmonic is about 3%. When the gap increases to $\frac{\lambda}{5}$, high order harmonics decay to zero. However, the magnitude of fundamental component also reduces to 35% of that at $\frac{\lambda}{30}$, as shown in figure 3-8, which could lead to higher power consumption of planar motor if working at this distance. As a compromise, planar motor has to fly at lower gap with 5^{th} and 9^{th} harmonics.

3.1.4 Force Ripple of M-Magnet array

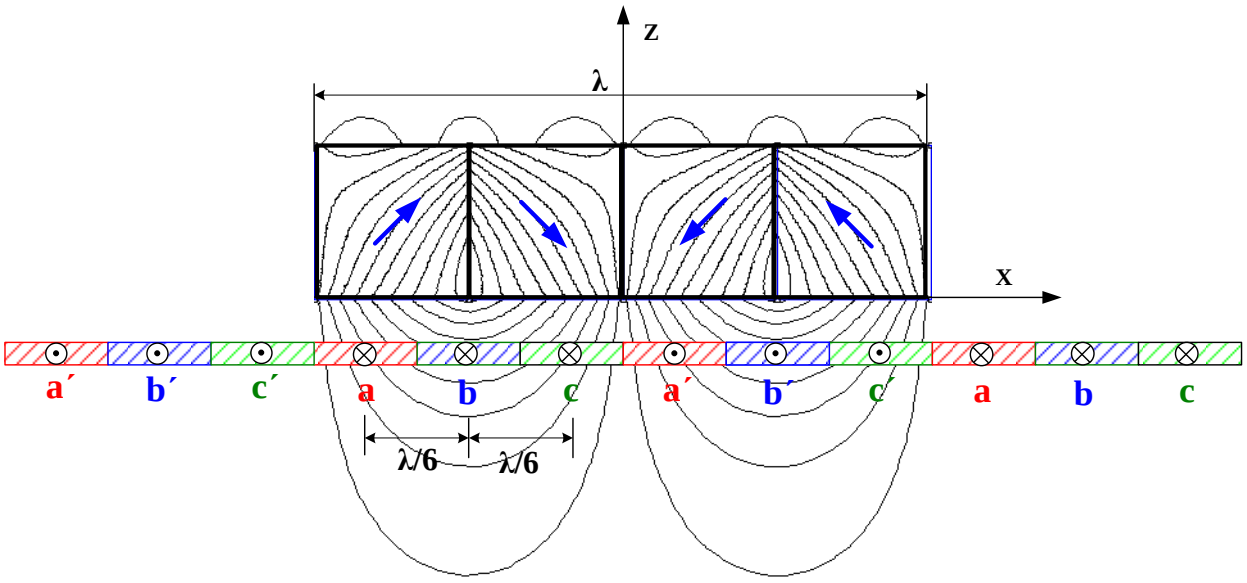

Figure 3-9 Magnetic field of M-Magnet array interacts with three phase currents

From [12][17][32], modulated current I_a can be used to generate 2D forces, F_x and F_z, for single M-Magnet array, which is given by

$$I_a = -I_{xr} e^{-\frac{z}{\lambda_1}} \cos(\frac{x}{\lambda_1}) - I_{zr} e^{-\frac{z}{\lambda_1}} \sin(\frac{x}{\lambda_1}) \qquad (3.5)$$

where $\lambda_1 = \frac{\lambda}{2\pi}$ is the fundamental component of magnetic field, I_{xr} and I_{zr} are the force commands to generate F_x and F_z exerting on magnet array respectively. I_b and I_c have $\frac{\pi}{3}$ and $\frac{2\pi}{3}$ phase delay relative to I_a, and I_a', I_b' and I_c' are inverse of I_a, I_b and I_c respectively. By applying Lorenz force law (2.47), we can derive that 5th and 9th harmonics will result in 6th and 10th force ripples, and 6th force ripples are dominant. More discussions about 6th force and torque ripples will be presented in section 3.2.

To attenuate high order force ripples due to conventional Halbach array, Usman [20] uses array splitting method to attenuate 6th force ripples. But this will lead to 5% force constant

reduction and increase array assembly complexity. A novel M-Magnet array layout is presented in this thesis to diminish high order force ripples without above trade-offs.

3.2 Array Layout

3.2.1 Single M-Magnet Array Layout for 2D Actuation

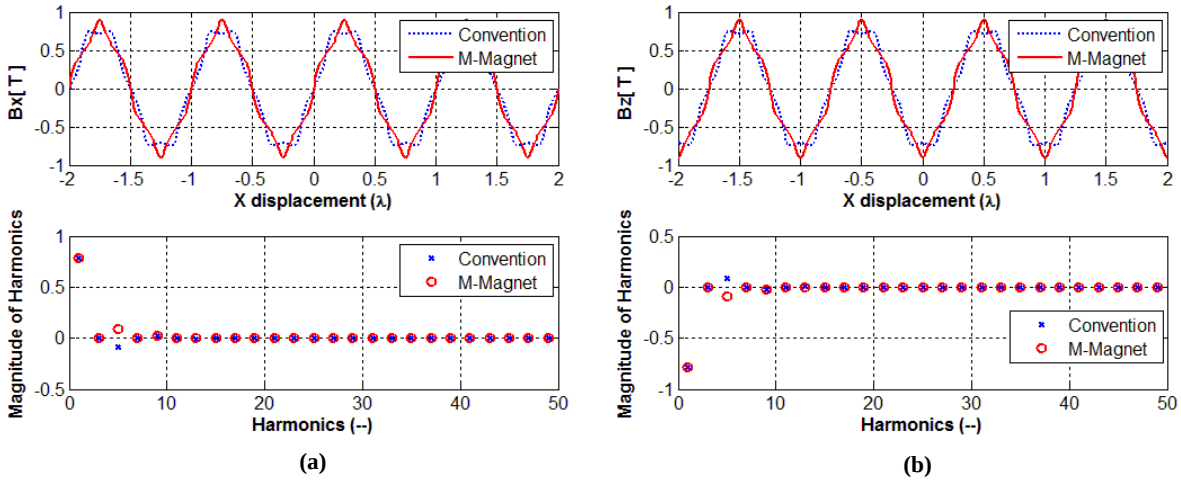

Figure 3-10 Comparison between conventional Halbach array and M-Magnet array (a) magnetic flux density in x-direction (Bx) (b) magnetic flux density in z-direction (Bz)

If we compare the 2D analytical field of conventional Halbach array (figure 2-3) with M-Magnet array (figure 3-7), it's noticed that 5^{th} harmonics of magnetic field in these two arrays have opposite sign for magnetic flux density in both x and z directions, as shown in figure 3-10 (a) and (b) respectively. Therefore, combining them together can perfectly cancel out 5^{th} harmonic; consequently 6^{th} force ripples can be removed.

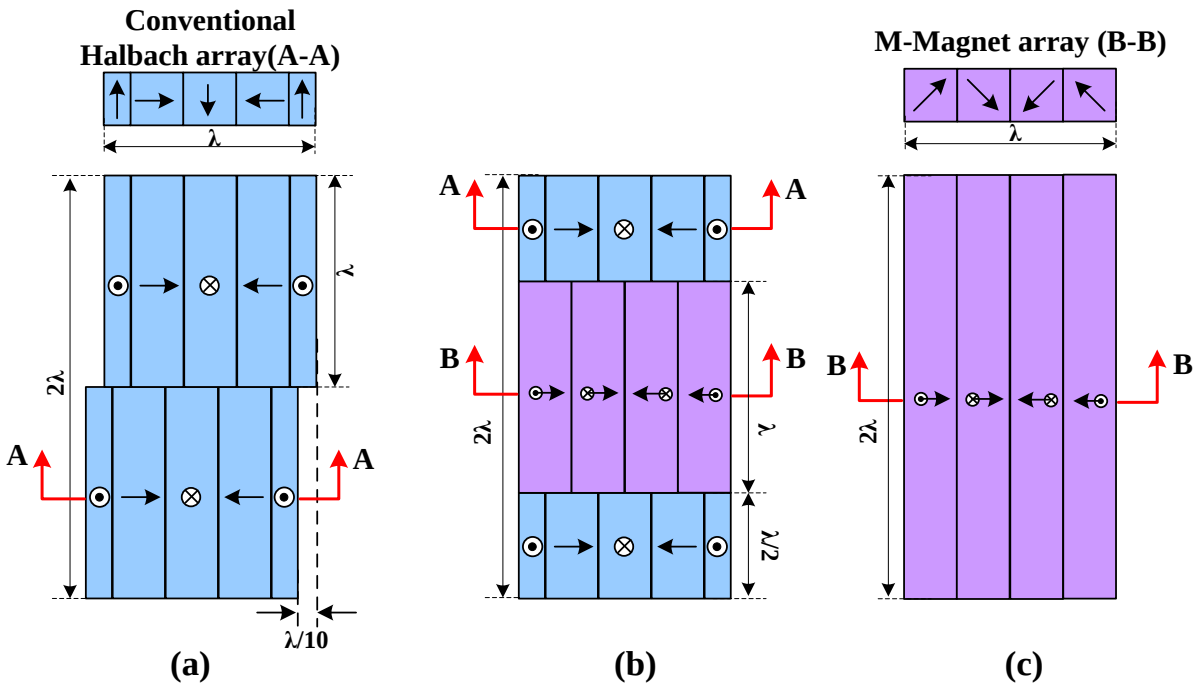

Figure 3-11 Single array layout (a) Split Array, adapted from [20]; (b) Hybrid array; (c) M-Magnet array

In figure 3-11, there are three types of magnet array: 1) conventional Halbach array with $\frac{\lambda}{10}$ shift along x direction between two halves of array cut in elongation direction (figure 3-11a); 2) one piece of M-Magnet array with λ width and 2λ length (figure 3-11c); 3) Hybrid magnet array consists of one M-Magnet array with λ width and λ length in the middle, two segments of conventional Halbach array with λ width and half λ length placed on two ends of the M-Magnet array respectively along y direction (figure 3-11b). To compare the performance of different array layouts, we can substitute (3.2) and (3.5) into (2.53)-(2.57), then 2D forces and 3D torques can be achieved for different array configurations.

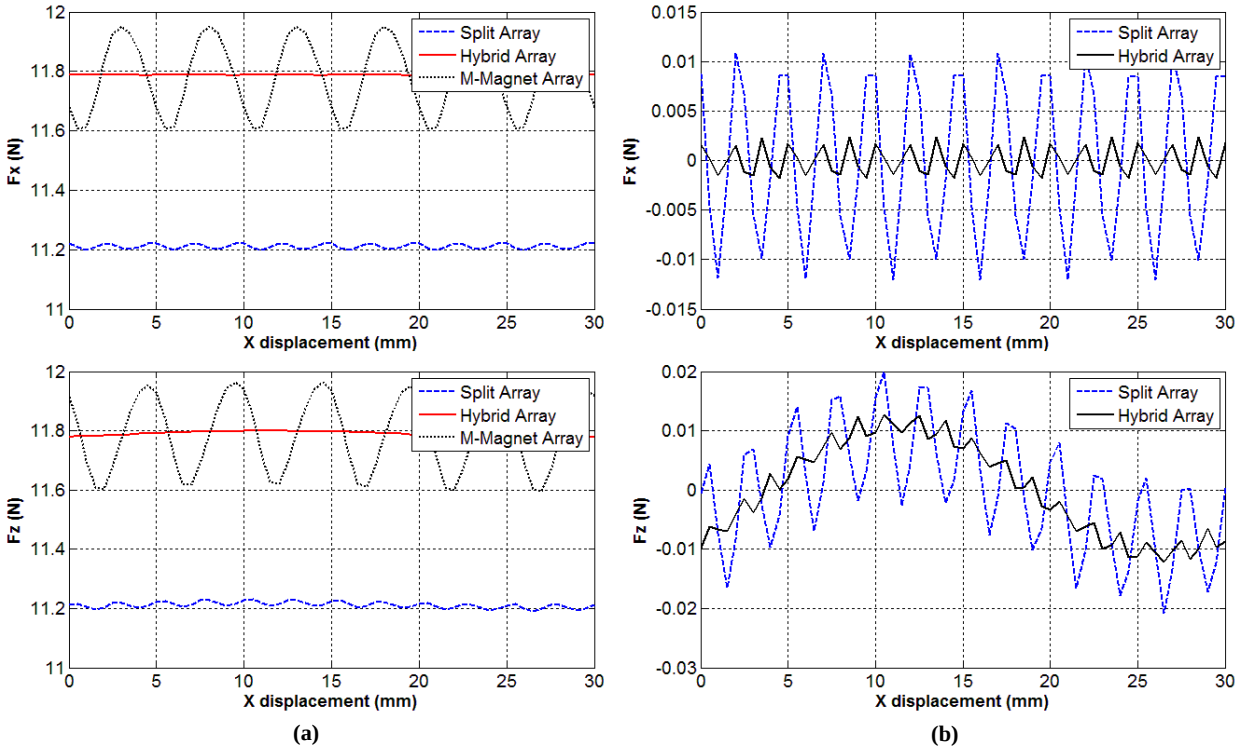

Figure 3-12 2D force comparison between different array layouts under same conditions ($z = -\frac{\lambda}{30}, I_{xr} = 10A, I_{zr} = 10A, 8\ turns\ of\ stator\ coils$) (a) mean force of Fx and Fz at array CG; (b) force ripple remnant comparison between Split array and Hybrid array after removing the mean force

Figure 3-12 shows that new hybrid array can achieve the best performance among three different layouts. First of all, no force constant reduction compared to split array, which has 5% force losses in both in-plane dragging force and out-plane levitation force as a compromise to attenuate 6th force ripples [20], shown in left plots of figure 3-12. Furthermore, 6th force ripples are totally cancelled out compared to pure M-Magnet array, whose 6th force ripples are about 1.3% of the mean force. Although split array can reduce the force ripple by a factor of 10, 0.1% higher-order force ripples (12th) still remain. Whereas hybrid array can achieve even smaller force ripples than split array, another factor of 10 force ripple reduction makes the remnants of force ripple only 0.01%.

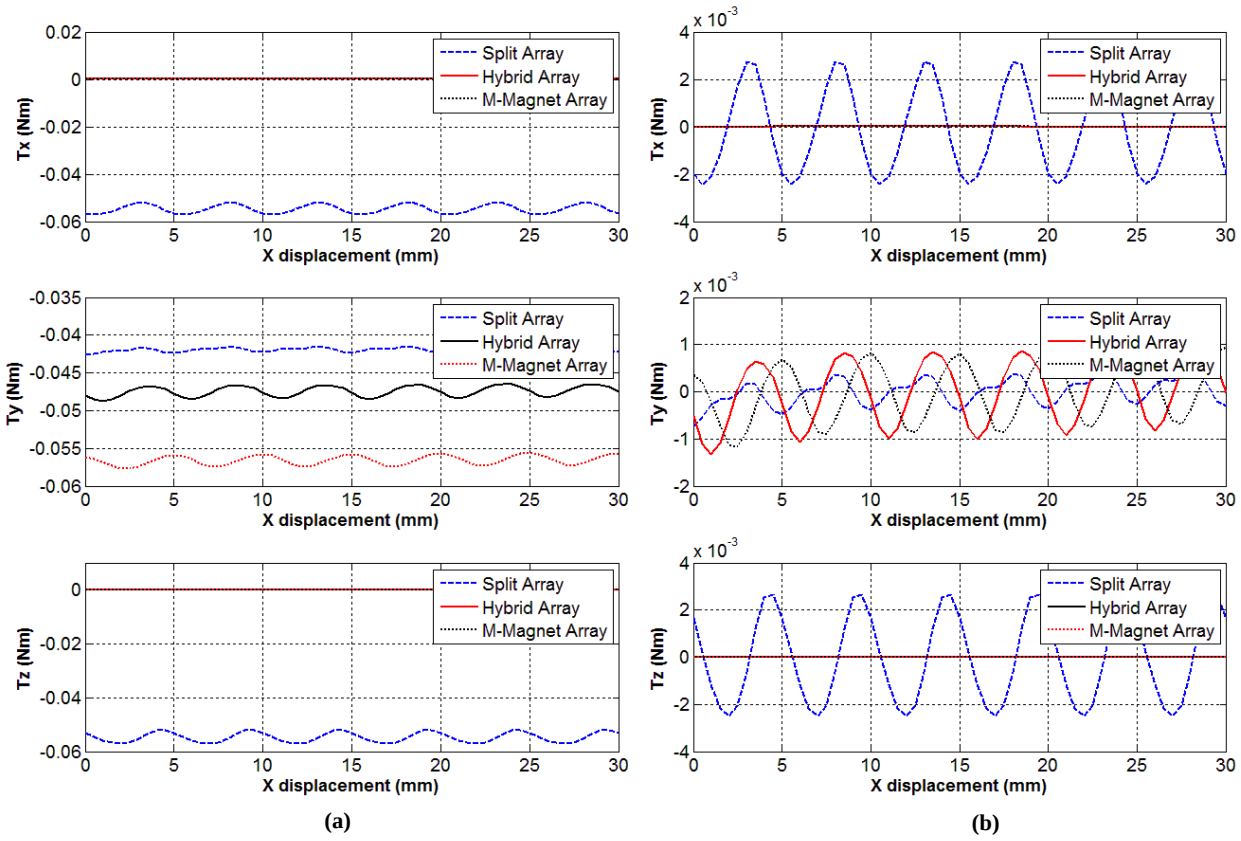

Figure 3-13 Torque comparison between different array layouts under same conditions ($z = -\frac{\lambda}{30}, I_{xr} = 10A, I_{zr} = 10A, 8\ turns\ of\ stator\ coils$) (a) Net torque around x, y and z-axis; (b) torque ripples after removing the mean force

On the other hand, if we look at the net torques around CG of different arrays in figure 3-13, it can be seen that split array has torque offsets and torque ripples around x, y, and z-axis due to asymmetric layout about x and y-axis, whereas M-Magnet array and hybrid array have zeros toques around x and z-axis. All of three arrays have torque offsets around y axis due to the offset translation force (Fx) relative to CG of magnet array. Although multiple arrays grouping in [17] can be used to mitigate the net torque of split array, this will lead to very complex mover assembly. Further, all of three arrays have 6th torque ripple around y axis.

In sum, from torque ripple point of view, pure M-Magnet array and hybrid array are better than split array since there are no torque ripples around x and z-axis. Although these two arrays still have 6^{th} torque ripple around y, it's decoupled with x and z-axis. Therefore, it can be easily compensated by control algorithm. Single split array cannot cancel out any of 6^{th} torque ripples around x, y and z-axis. Hence specific array combination is required to deal with torque ripples [17] for planar motor design with split array. The 6^{th} force and torque ripples of three different array patterns are summarized in Table 3.1 along with the mean levitation and translation forces.

Table 3-1 Force and torque comparison between different array patterns

array layout	*mean force (N)*		*6th force ripple(p-p,N)*				*mean torque(Nm)*			*6th torque ripple (Nm)*		
	Fx	*Fz*	F_{x6}	*%*	F_{z6}	*%*	*Tx*	*Ty*	*Tz*	T_{x6}	T_{y6}	T_{z6}
Split array	11.2	11.2	0.023	0.21	0.023	0.21	-0.055	-0.042	-0.055	0.0052	0.0012	0.0052
MM array	11.787	11.79	0.345	2.93	0.369	3.13	8E-05	-0.057	-2E-05	0	0.0022	0
Hybrid array	11.788	11.789	0.0041	0.03	0.0045	0.04	8E-05	-0.047	-2E-05	0	0.0023	0

3.2.2 M-Magnet Array Layout for 6D Actuation

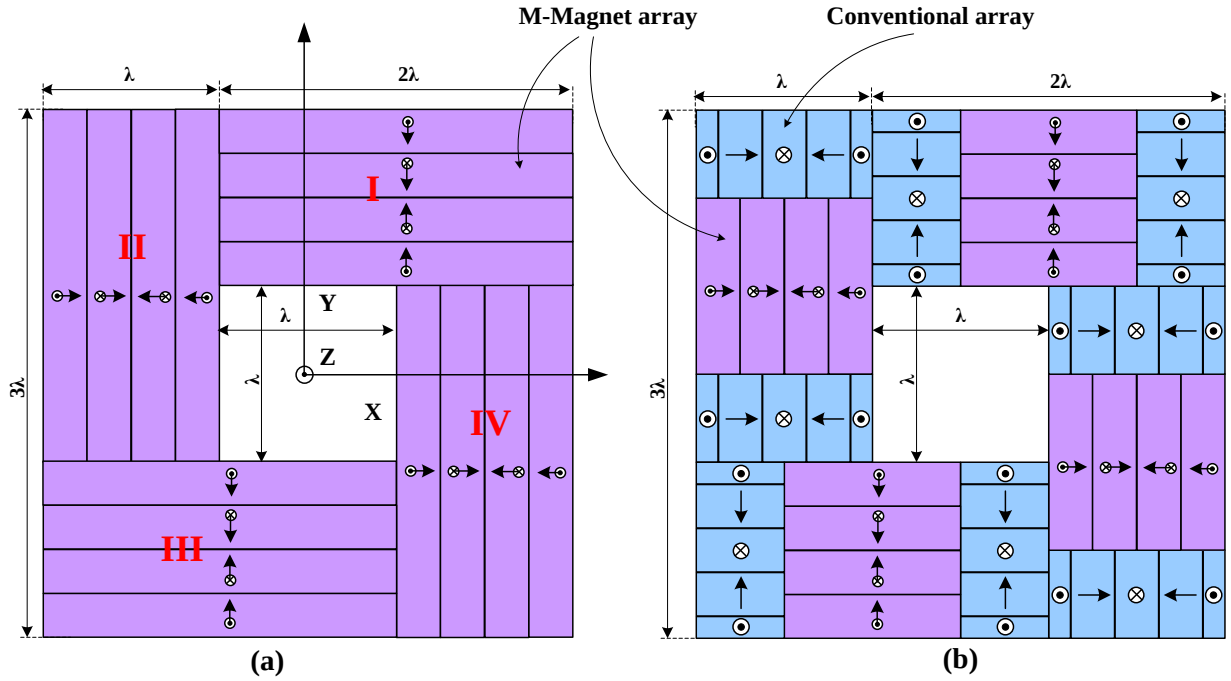

Figure 3-14 M-Magnet array layout for six degree of freedom actuation (a) Pure M-Magnet mover; (b) Hybrid M-Magnet mover

Based on previous work in [12], four identical M-Magnet arrays are grouped to generate six degree of freedom actuation, as shown in figure 3-14a. Array I and III are elongated in x direction, each array generates translation force in y-axis and levitation force in z-axis respectively; Array II and IV are elongated in y direction, each array generates translation force in x-axis and levitation force in z-axis respectively. Totally, 8 individual forces are combined to drive the mover with 6DOF motion. According to the analysis in section 3.2.1, we can have at least two mover configurations: 1) Pure M-Magnet mover consists of four M-Magnet arrays, each one has one λ in width and two λ in length respectively. This is the simplest layout with only one type of magnet. Thus it's very cost effective and easy to be built. However, 6^{th} force ripples in x, y and z-axis and torque ripples around x and y-axis will degrade the performance of

the planar motor when it's applied to high precision machines, for instance lithography tools; 2) Another mover layout is using four hybrid arrays to generate 6D actuation shown in figure 3-14b. This configuration can achieve much better performance for high accuracy application since all of 6^{th} force ripples in x, y and z-axis and torque ripples around z-axis are eliminated. Only 6^{th} torque ripples around x and y axes remain, but they are decoupled. Hence, it's easy to be compensated by control algorithm.

Figure 3-14 shows a very compact mover configuration with high filling factor, 89% of area is magnet. Because four arrays tightly connect with each other to create a perfect square without any gap between neighbors, this layout can be easily generalized as pattern in figure 3-15. In which, $n \times n$ M-Magnet arrays or Hybrid arrays placed in same elongation direction to form a group, each array group has $n\lambda$ in width and $2n\lambda$ in length respectively, total square side length of the mover is $3n\lambda$, where $n = 1,2,3, \dots, N$. By properly choosing integer number of n, various size of mover can be achieved with same acceleration capability, which has only one type of magnet for low performance application, and four types of magnet for high performance application.

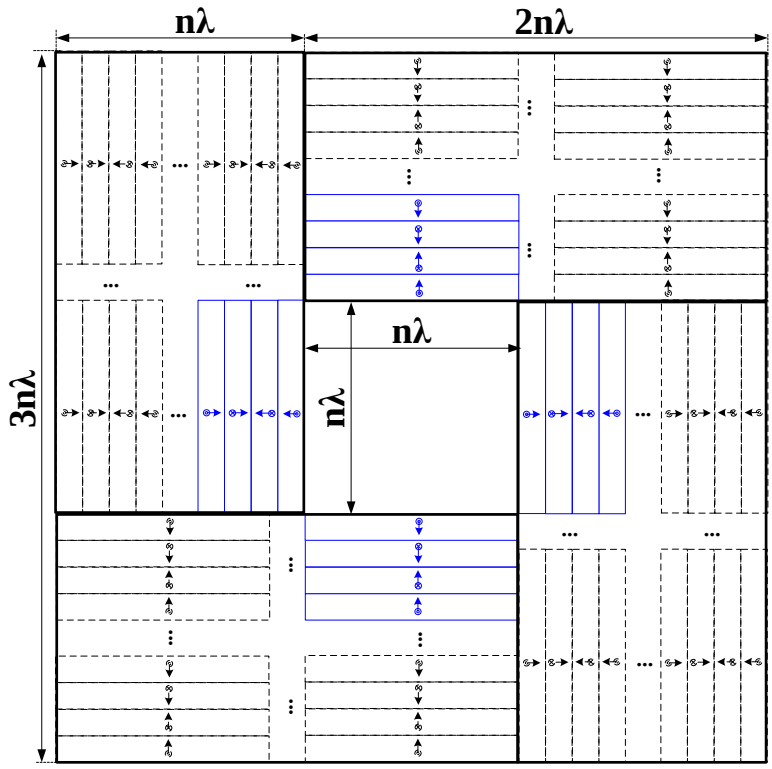

Figure 3-15 General M-Magnet array layout for various mover size

3.3 Manufacturing Tolerances of M-Magnet Array

From manufacturing point of view, 45 degree magnetization of M shape magnet could result in big angle error compared to 90 degree magnetization of conventional NS magnets. Even if the error can be controlled within a small range, this could lead to much higher fabrication cost. This section will investigate how sensitive of magnetization angle error is relative to the actuation performance of M-Magnet array. In addition, geometric tolerances of magnet are also investigated for the same purpose.

3.3.1 Magnetization Angle Tolerance

Calculation inputs:

- Magnetization angle error from $\pm 1^0$ to $\pm 10^0$ will be used to investigate the relationship between angle tolerance and actuation performance of M-Magnet array.

- For each angle error E, 20 times of 2D-force and ripple calculation of single array are performed.
- For each force and ripple calculation, angle error will be randomly selected within the range of $\pm E$.
- Mean forces and 6th force ripples of M-Magnet array from table 3-1 are used as reference of comparison.

Calculation outputs:

- Maximum deviation from reference among 20 times calculations of each angle tolerance is recorded, including mean forces F_x and F_z and 6th force ripples F_{x6} and F_{z6}, as shown in table 3-2.

Table 3-2 Mean force and 6th force ripple deviation for various angle tolerances [1]

angle tolerance (degree)	*mean force(N)*		*6th force ripple (N)*		$\frac{100\times\lvert F_x - F_{xr}\rvert}{F_{xr}}$	$\frac{100\times\lvert F_z - F_{zr}\rvert}{F_{zr}}$	$\frac{100\times\lvert F_{x6} - F_{xr6}\rvert}{F_{xr6}}$	$\frac{100\times\lvert F_{z6} - F_{zr6}\rvert}{F_{zr6}}$
	Fx	*Fz*	*Fx6*	*Fz6*				
0	11.787	11.791	0.3446	0.3686	0.0	0.0	0.0	0.0
1	11.877	11.699	0.3438	0.3676	0.8	0.8	0.2	0.3
2	11.532	12.04	0.346	0.3665	2.9	2.9	0.6	0.3
3	11.48	11.481	0.342	0.3659	2.6	2.6	0.8	0.7
4	11.385	12.163	0.348	0.3651	3.4	3.2	1.0	0.9
5	11.078	11.113	0.3478	0.3647	6.0	5.8	0.9	1.1
6	12.431	11.097	0.342	0.373	5.5	5.9	0.8	1.2
7	12.497	11.003	0.342	0.3738	6.0	6.7	0.8	1.4
8	10.672	12.799	0.349	0.374	9.5	8.5	1.3	1.5
9	10.877	10.827	0.349	0.362	7.7	8.2	1.3	1.8
10	10.235	13.126	0.351	0.375	13.2	11.3	1.9	1.7

[1] Calculation conditions are the same as section 3.2: $z = -\frac{\lambda}{30}, I_{xr} = 10A, I_{zr} = 10A, 8\ turns\ of\ stator\ coils$

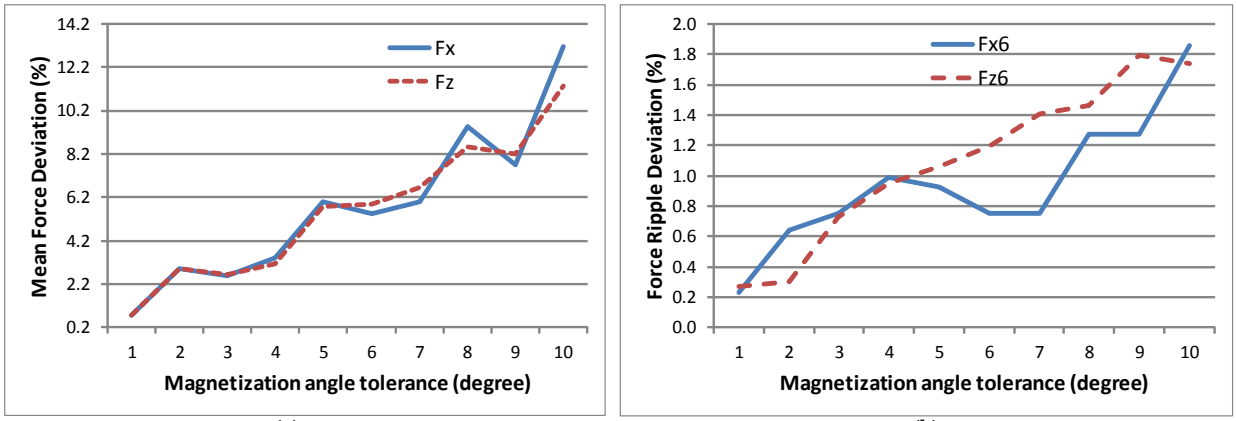

Figure 3-16 (a) Mean force deviation against angle tolerance; (b) 6th force ripple deviation against angle tolerance

Conclusions:

- Figure 3-16 shows that thrusting and levitation forces and corresponding 6th force ripples of M-Magnet array are proportional to magnetization angle tolerance.
- Mean force deviation is much bigger than force ripple when angle tolerance increases, it goes to 13% at $\pm 10^0$ angle error shown in figure 3-16a. Whereas, the deviation is less than 2% for 6th force ripples with the same angle error shown in figure 3-16b.

3.3.2 Magnet Geometric Tolerances

Magnet Length tolerance

According to Lorenz force law (2.47), actuation forces of magnet array are proportional to the length of magnet. If we take 2λ (60mm) length as example, $200\mu m$ tolerance only result in 0.3% force deviation for both mean force and 6th force ripple.

Magnet Height tolerance

From (2.44) and (2.45), it's noticed that magnetic flux density is proportional to $(1-e^{-\frac{h_m}{\lambda_n}})$. Similarly, if taking $h_m=\frac{\lambda}{4}$ (7.5mm) as example, $200\mu m$ tolerance leads to only 1% deviation of mean force and 0.01% of 6th force ripple respectively.

Magnet Width tolerance

Magnet width tolerance is more complex than other two dimensions, which is related to the shape of magnetic field. Similarly as magnetization angle tolerance analysis, 4 different width tolerances, $50\mu m$, $100\mu m$, $150\mu m$ and $200\mu m$, are used as the inputs of 2D force and ripple calculation of single array. 20 times of calculation are performed for each width tolerance, and maximum deviation relative to the width tolerance is recorded to compare with reference mean forces and force ripples. Calculation results are listed in table 3-3.

Table 3-3 Mean force and 6th force ripple deviation for various width tolerances[2]

width tolerance (μm)	*mean force(N)*		*6th force ripple (N)*		$\frac{100\times\lvert F_x-F_{xr}\rvert}{F_{xr}}$	$\frac{100\times\lvert F_z-F_{zr}\rvert}{F_{zr}}$	$\frac{100\times\lvert F_{x6}-F_{xr6}\rvert}{F_{xr6}}$	$\frac{100\times\lvert F_{z6}-F_{zr6}\rvert}{F_{zr6}}$
	Fx	*Fz*	*Fx6*	*Fz6*				
0	11.787	11.791	0.3446	0.3686	0.00	0.00	0.00	0.00
50	11.858	11.872	0.3377	0.3607	0.60	0.69	2.00	2.14
100	11.608	11.638	0.325	0.347	2.11	1.97	3.76	3.80
150	11.5927	11.5927	0.368	0.346	1.65	1.68	6.79	6.13
200	11.524	11.529	0.313	0.335	2.23	2.22	9.17	9.12

Conclusions

Deviations of different geometric tolerances in length, height and width respectively are summarized in table 3-4.

[2] Calculation conditions are the same as section 3.2: $z=-\frac{\lambda}{30}, I_{xr}=10A, I_{zr}=10A, 8\ turns\ of\ stator\ coils$

Table 3-4 Mean force and 6th force ripple deviation for different geometric tolerances

Geometry	*Deviation (%)*	*tolerance (μm)*			
		50	*100*	*150*	*200*
length	**mean force**	0.08	0.17	0.25	0.3
	force ripple	0.08	0.17	0.25	0.3
height	**mean force**	0.3	0.6	0.8	1.1
	force ripple	0.002	0.004	0.007	0.009
width	**mean force**	0.69	2.11	2.28	3.22
	force ripple	2.14	3.8	6.79	9.17

- From table 3-4, it can be seen that length tolerance has very small contribution to mean force and force ripple deviation compared to other two geometric tolerances.
- Mean force deviation due to height tolerance is much bigger than force ripple, which is proportional to the tolerance. When magnet manufacturing has $200\mu m$ height error, mean force deviation is around 1%, whereas force ripple deviation is negligible.
- Both force and ripple deviations are proportional to width tolerance. As width tolerance affects the shape of magnetic field, deviation of force ripple is about 3 times bigger than mean force, which reaches 9% at $200\mu m$ tolerance. Whereas, it's only 3% for mean force deviation with same tolerance.

In sum, from actuation point of view, to balance the fabrication cost and performance of M-Magnet array in overall, following tolerances are chosen: 1) $\pm 2^0$ magnetization angle tolerance; 2) $\pm 150\mu m$ tolerance for both height and width of magnet cross section; 3) $\pm 150\mu m$ or more tolerance for the length of magnet.

3.4 Array Assembly

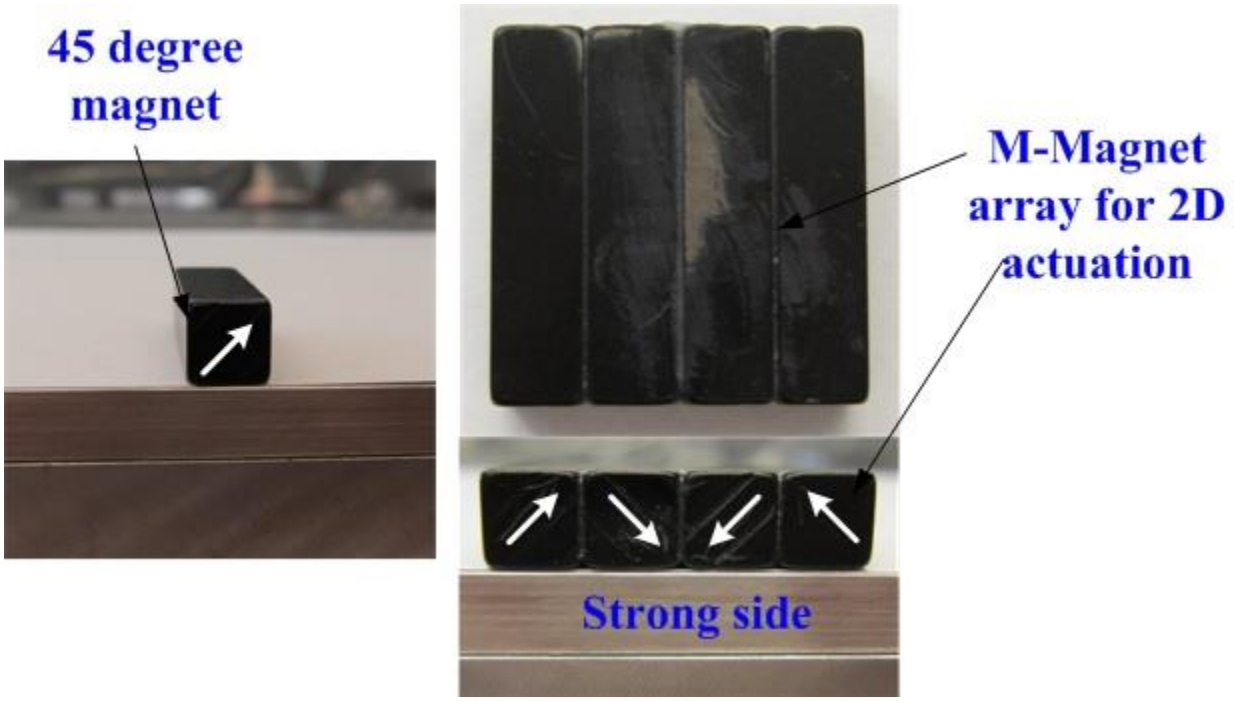

Figure 3-17 M-Magnet array assembly for 2D actuations

Figure 3-17 shows the M-Magnet array assembly for 2D actuations. To compare with conventional Halbach array in [17], M-Magnet array assembly is much easier because every single magnet is identical. We don't need to worry about misplacing of magnets during array assembly. Furthermore, we can easily manipulate two pieces of magnets at each half of M-Magnet array due to attraction force between them. The only effort is to push two halves of M-Magnet array against each other by much simpler assembly jig compare to conventional Halbach array assembly in [17]. Consequently, array assembly of M-Magnet array is more efficient than conventional Halbach array.

Chapter 4: Experiment

In this chapter, magnetic field of a fabricated M-Magnet array with $\lambda = 30mm$ length is tested at two different heights on the strong side of the array. To be comparable with the calculation results from 3D magnetic surface charge model in section 3.1.2, one distance from the surface of strong side of M-Magnet array is at $z = -\frac{\lambda}{30} = -1mm$, which is close to the magnet array; another distance is at $z = -\frac{\lambda}{5} = -6mm$, which is far away from the magnet array. But for actual experimental set-up, these values are adapted to $z = -1.3mm$ and $z = -6.5mm$ respectively. On the other hand, geometric tolerance of the width due to magnet manufacturing needs to be taken into account to correct the 3D analytical model of M-Magnet array. Otherwise, the experiment error between distorted actual magnetic field and undistorted magnetic field model is more than 10%. After field correction, this error can be reduced to 3%.

4.1 Experiment Set Up

Figure 4-1a shows the overview of experiment set-up for magnetic flux density test of M-Magnet array. Here Gaussmeter of Model 7010 with different ranges (300mT/3T) and 1mT resolution is used to measure magnetic field at the strong side of M-Magnet array. In this experiment, only magnetic flux density in z-axis (Bz) is measured since it's easier to be detected compared to magnetic flux density in x-axis (Bx). On the other hand, to be comparable with the calculation results in chapter 3, magnetic fields at different distances from the surface of strong side of M-Magnet array, $z = -\frac{\lambda}{5}$ and $z = -\frac{\lambda}{30}$, are tested, which have different experiment set-ups as shown in figure 4-1b and figure 4-1c. For long distance ($z = -\frac{\lambda}{5}$) test, magnet array is attached to a transparent plastic spacer with 5.1mm thickness. On top of the spacer, a transparent plastic grid shown in figure 4-2a is applied to align Gaussmeter probe and magnet array. For short

distance ($z = -\frac{\lambda}{30}$) test, magnet array is bound to the plastic grid directly. After that the whole piece is bound to a supporting base to enhance the set-up.

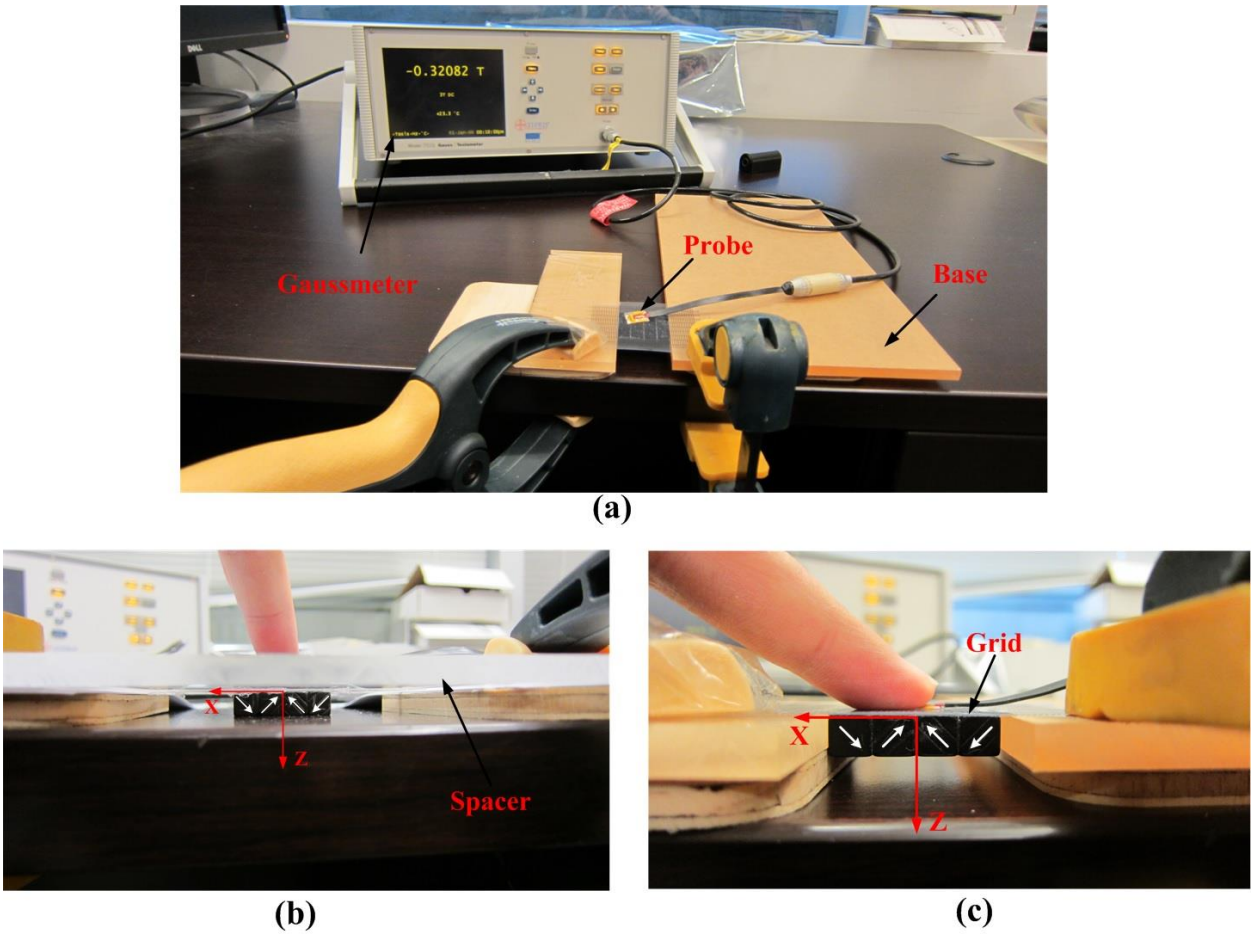

Figure 4-1 (a) Overview of magnetic flux density measurement of M-Magnet array; (b) Set-up for field measurement at $z = -\frac{\lambda}{5}$; (c) Set-up for field measurement at $z = -\frac{\lambda}{30}$

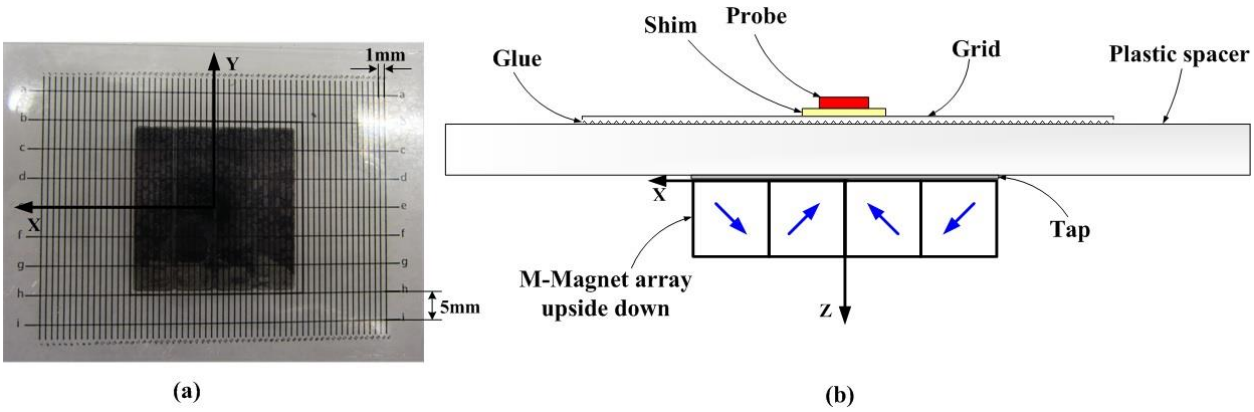

Figure 4-2 (a) Plastic grid (b) Overview of experiment set-up in z direction

According to the feature of Bz in figure 3-3, various resolutions are used to measure the field, which are 1mm in x-axis and 5mm in y-axis respectively, to reduce the test points, as shown in figure 4-2a. Further, the test range is also different for lateral direction (x) and elongation direction of magnet array, which is $\pm 30mm$ in x-axis and $\pm 20mm$ in y-axis respectively. To obtain various test distances on the strong side of M-Magnet array, a plastic spacer is applied along with other additional parts that contribute to the actual measurement height. All of these parts separating magnet array and probe are listed in table 4-1 for different test heights.

Table 4-1 Actual height of magnetic field test

	actual height of high level test (mm)	*actual height of low level test (mm)*
Probe	0.508	0.508
Shim	0.55	0.55
Grid	0.1	0.1
Glue	0.1	-
Spacer	5.1	-
Tap	0.1	0.1
Coating	0.02	0.02
Total	**6.478**	**1.278**

From table 4-1, it can be seen that the actual heights for high level and low level test are around 6.5mm and 1.3mm respectively instead of $|z| = \frac{\lambda}{5} = 6mm$ and $|z| = \frac{\lambda}{30} = 1mm$. Therefore, the field comparison between 3D analytical model and experiment results are based on actual heights.

4.2 Experimental Results of M-Magnet Array

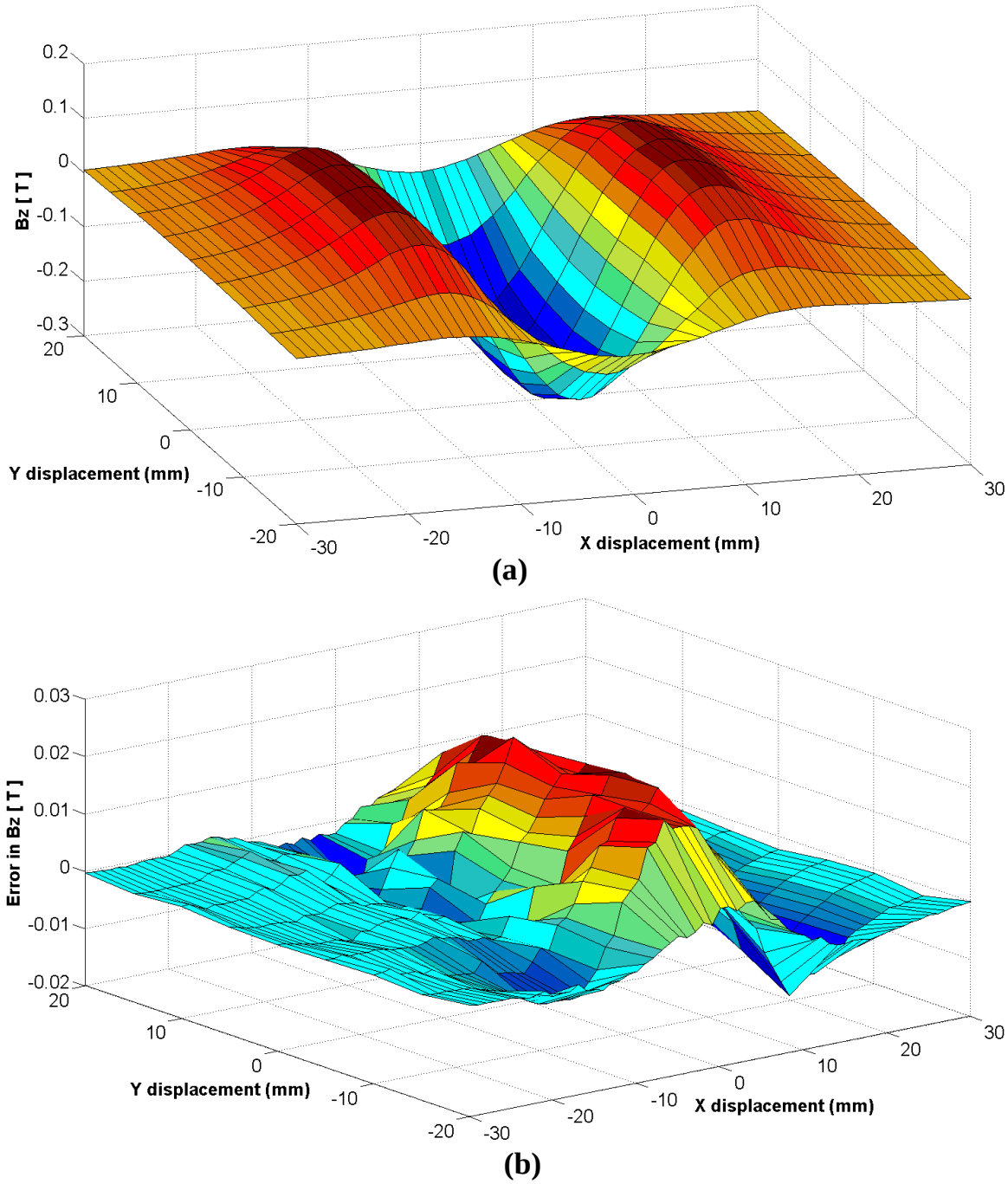

Figure 4-3 Experimental 3D magnetic field of M-Magnet array under the conditions: $\lambda = 30mm$, $h_m = 7.5mm$, $L_m = \lambda$, $B_r = 1.36T$ and $z = -6.5mm$ (a) Measured magnetic field of Bz (b) Field Error in Bz ($Error = B_{Exp} - B_{3DMM}$)

Figure 4-3a shows the measured magnetic field of single M-Magnet array with $30mm$ length at the distance of $z = -6.5mm$. To compare with the analytical results from 3D magnetic surface charge mode (3DMM) at the same distance, field error is calculated in figure 4-3b. Maximum error is about 8%, which comes from the middle region around $x = 0$. If we look at the shape of the error field, this is related to the actual magnetic field itself instead of experiment error path in table 4-1.

As discussed in section 3.3, from magnetic field point of view, geometric tolerances of magnet dominate the field error, especially the width tolerance which directly affects the shape of magnetic field. The contributions to the field error from length and height tolerances are less than 1%, hence they are negligible. After correcting the 3D analytical field by the real width of magnet, which is $7.44 - 0.15mm$, new field error is plotted in figure 4-4. To generalize the width affection, simulated width of four magnet pieces are reduced by 0.15mm to correct the analytical magnetic field of Bz.

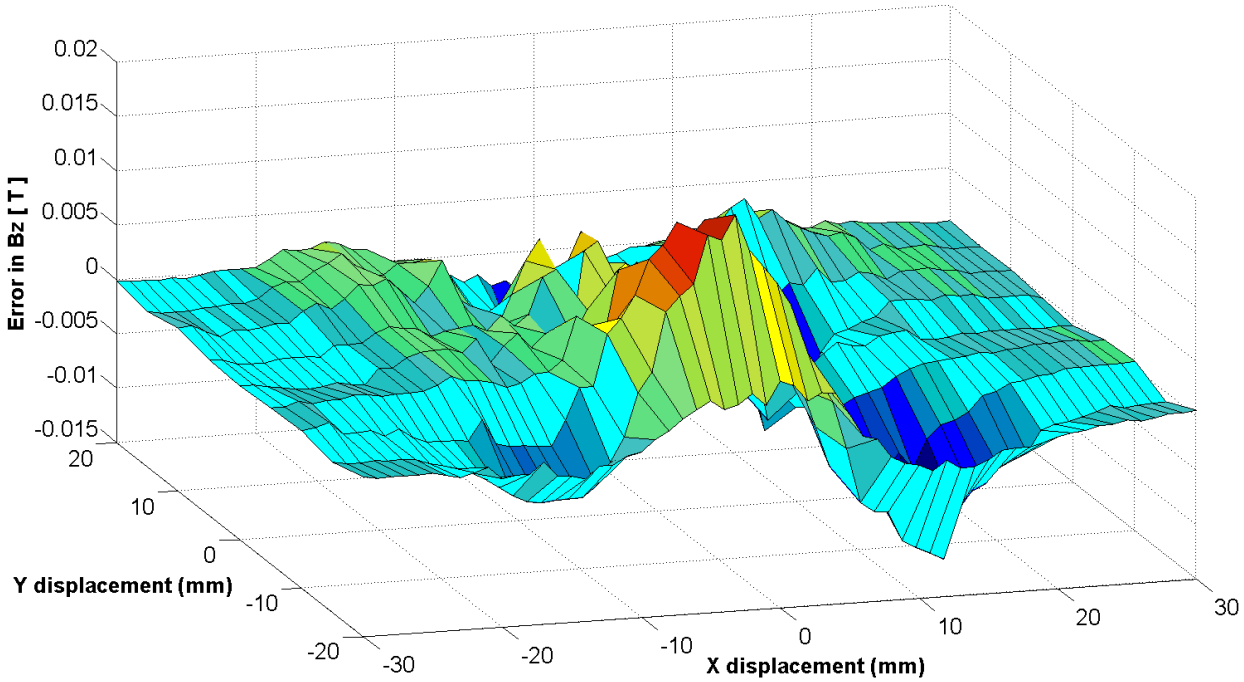

Figure 4-4 Field error after 0.15mm width correction to 3DMM at $z = -6.5mm$

After field correction, field error between experiment results and corrected 3D analytical model is less than 3% at most of the test region. But at a small region of the third quadrant, the error is still greater than 5%, which is related to the unexpected gap due to air bubble inside the tap. If we only look at the 2D magnetic field at y=0, analytical results by 3D magnetic surface charge model is matched with experimental results, maximum error is less than 3%, as shown in figure 4.5.

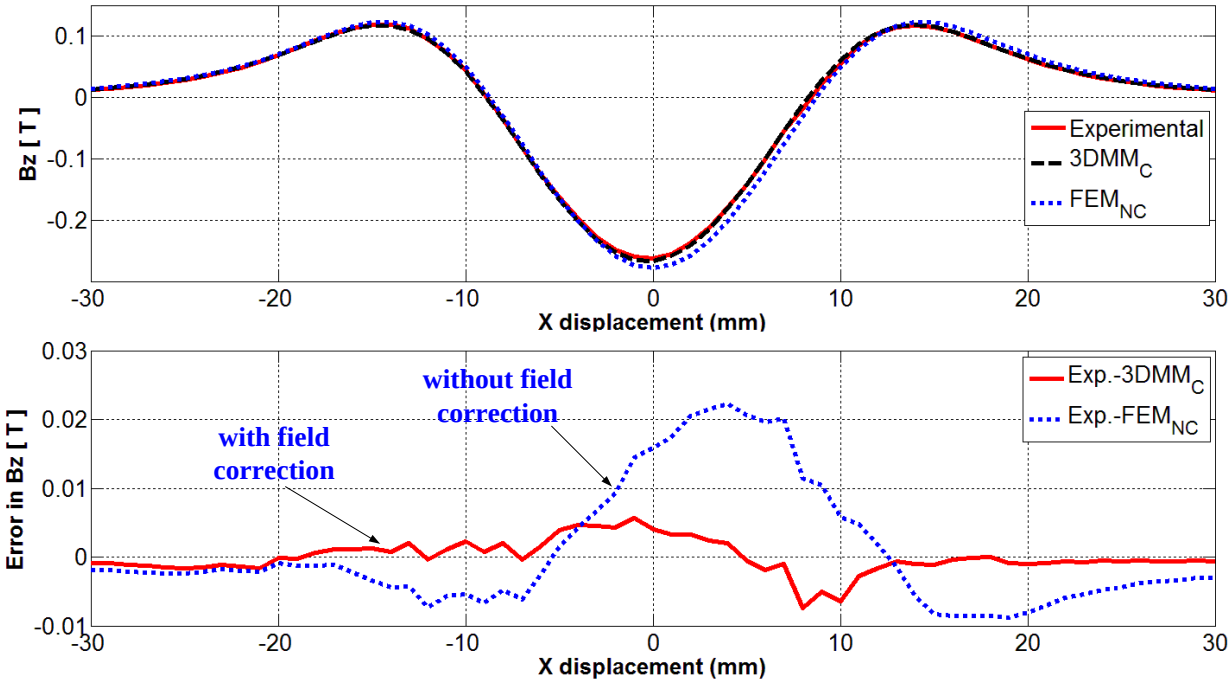

Figure 4-5 Comparison of experimental field, 3DMM field with field correction and FEM field without field correction at $y = 0$ and $z = -6.5mm$

According to the 3D analytical magnetic field analysis in section 3.1.2, the error of analytical model with respect to FEM is less than 1%. Therefore, we can use FEM result as reference to compare the difference before width correction and after width correction. In figure 4-5, 2D magnetic fields of Bz by experiment, 3D analytical model with width correction ($3DMM_C$) and FEM model without width correction (FEM_{NC}) are plotted. Apparently, 3D analytical model can match experimental results very well after correcting the width error of magnet. Maximum field error is reduced from 8.3% to 2.6%.

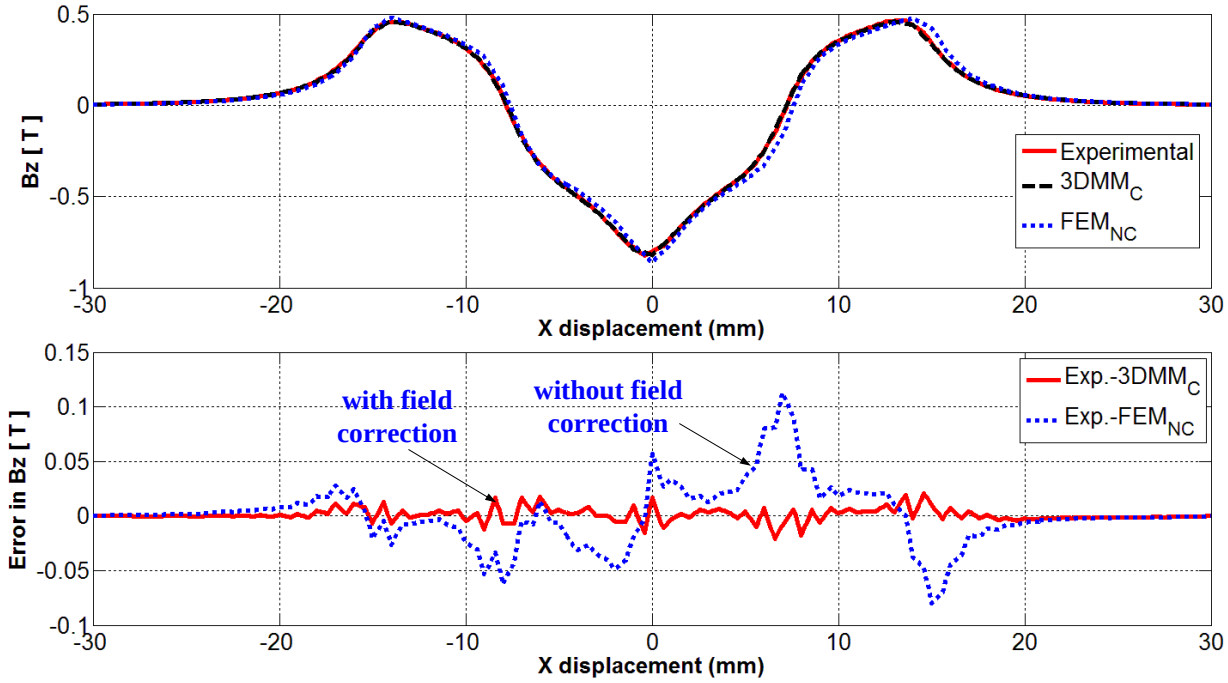

Figure 4-6 Comparison of experimental field, 3DMM field with field correction and FEM field without field correction at $y = 0$ and $z = -1.3mm$

Similarly for low level test at $z = -1.3mm$, field error between experimental results and 3D analytical model decreases from 13.7% without width correction to 2.5% with width correction, as shown in figure 4-6. Again, 3D analytical model matches experimental results very well at near distance to the magnet.

Chapter 5: Conclusion

5.1 Novel M-Magnet Array

This thesis presented a novel M-Magnet array. Analytical models were developed to calculate the magnetic field of M-Magnet array and the force generated by the magnetic field interacting with stator coils. Experimental measurements confirmed the developed analytical models.

Two magnetic field calculation tools are developed. One is 3D magnetic field modeling based on magnetic surface charge model, which is convenient for the analysis of rectangular prim magnets. Furthermore, 3D magnetic field modeling of magnet is much faster than finite element (FEM) simulation in COMSOL, and the simulation error between 3D analytical model and FEM is less than 1%. Another tool is 2D magnetic field modeling based on Fourier series, which mainly focuses on the harmonics of magnet array. Whereas these harmonics are the sources of high order force ripples when combing with three-phase commutation law. Force and torque models are also developed based on numerical integration of Lorenz force, which are very convenient for the magnet array layout design and manufacturing tolerance analysis of M-Magnet array.

M-Magnet array has several benefits compare to conventional Halbach array: 1) less magnet pieces for one spatial period to generate mirror-symmetric magnetic field about middle vertical axis, generally 5 pieces in [12][17] or 9 pieces in [31] are mostly used, whereas only 4 pieces for an M-Magnet array; 2) only one type of identical magnet piece makes array assembly much easier and faster, whereas for conventional Halbach array, thin and long side magnet piece always creates trouble for the array assembly. Furthermore, from manufacturing point of view, M-Magnet array is more cost effective due to uniform magnet configuration. On the other hand, hybrid array layout for 2D actuation based on M-Magnet array can perfectly cancel out 5^{th}

harmonic of pure M-Magnet array, which is the trouble maker of 6^{th} force ripple in planar motor design. Although existing solution in [20] based on conventional Halbach array can also attenuate 6^{th} force ripple by a factor of 10, there are some compromises coming along: 1) 5% force constant reduction; 2) increasing complexity of array assembly due to array splitting. However, there is one drawback for the new hybrid array, which cannot fully cancel out 6^{th} torque ripple around y-axis. But the 6^{th} torque ripple is decoupled between axes; therefore it can be easily compensated by control algorithm. Further, with uniform layout of single M-Magnet array, it's easy to build various sizes of mover with 6D actuation by only one type of magnet.

In addition, to balance the fabrication cost and actuation performance of M-Magnet array, magnetization angle tolerance and geometric tolerances are analyzed. Angle tolerance mainly affects the phase of magnetic field, which will cause 10% force constant reduction at 10^0 tolerance. But this could be compensated by current commutation. Geometric tolerances affect the overall field strength, among these tolerances width tolerance is dominant, which results in 3% force constant reduction and around 9% 6^{th} force ripple deviation at $200\mu m$ width manufacturing error.

To verify simulation results of M-Magnet array, magnetic field at two different heights around $z = -\frac{\lambda}{5}$ and $z = -\frac{\lambda}{30}$ are tested. After correcting the 3D analytical magnetic field by $150\mu m$ width error due to magnet manufacturing, calculation results can match experimental results with less than 3% error.

5.2 Future Work

Forces and torques generated by M-Magnet array are suggested to be tested by building an experimental platform combining with stator coils. Meanwhile, 6^{th} force and torque ripples could

also be tested at this platform. Furthermore, hybrid arrays can be built and tested to verify the actuation performance of hybrid array predicted by the analytical models.

By applying six degree of freedom position sensors such as [33] or [34], control performance of planar motor based on M-Magnet array could also be tested in terms of acceleration capability. To verify the performance improvement due to 6^{th} force ripple attenuation by hybrid array, more accurate 6D position sensors such as [35] have to be used to position the stage since tracking error due to 3% force ripple could be immersed into sensor noise in [33] or [34].

To verify the scalability of M-Magnet array, much bigger size of planar motor can be built, which will have the same acceleration capability and 6^{th} force ripple attenuation as small size mover in this thesis.

Bibliography

[1] W. T. Novak, Z. Premji, U. G. Nayak and A. Ebihara, "Precision motion stage with single guide beam and follower stage". US Patent 5623853 A 1997.

[2] E. R. Loopstra, G. M. Bonnema, H. K. Van Der Schoot, G. P. Veldhuis and P. M. Ter Beek, "Two-dimensional y balanced position device with two object holders, and lithography device provided with such a positioning device". US Patent 5969441 1999.

[3] K. Erkorkmaz, J. M. Gorniak and D. J. Gordon, "Precision machine tool X-Y stage utilizing a planar air bearing arrangement," *CIRP Annals-Manufacturing Technology*, vol. 59, no. 1, pp. 425-428, 2010.

[4] B. Sawyer, "MAGNETIC POSITIONING DEVICE". US Patent 3376578 1968.

[5] P. C. M. Frissen, J. C. Compter, M. J. M. Renkens, G. A. J. De Fockert and R. J. M. Coolen, "DISPLACEMENT DEVICE". US Patent 6661127 2003.

[6] F. de Jong, B. van der Pasch, T. Castenmiller, B. Vleeming, R. Droste and F. van de Mast, "Enabling the lithography roadmap: an immersion tool based on a Novel Stage Positioning System," *Optical Microlithography XXII Proceeding of SPIE*, vol. 7274, no. 1, pp. 72741S1-72721S10, 2009.

[7] D. A. Markle, "MAGNETICALLY-POSITIONED X-Y STAGE HAVING SIX-DEGREES FREEDOM". US Patent 5886432 1999.

[8] A. J. Hazelton, M. B. Binnard, and J. M. Gery, "Electric motors and positioning devices having moving magnet arrays and six degrees of freedom". US Patent 6,208,045 2001.

[9] M. Binnard, "PLANAR MOTOR WITH LINEAR COIL ARRAY". US Patent 6445093 2002.

[10] J. W. Jansen, C. M. van Lierop, E. A. Lomonova and A. J. Vandenput, "Magnetically levitated planar actuator with moving magnets," *IEEE Transactions on Industry Applications*, vol. 44, no. 4, pp. 1108-1115, 2008.

[11] J. C. Compter, P. C. M. Frissen, and J. Van Eijk. "Displacement device". US Patent 7,948,122 2011.

[12] X. Lu and I.-u.-r. Usman, "6D direct-drive technology for planar motion stages," *CIRP Annals - Manufacturing Technology*, vol. 61.1, pp. 359-362, 2012.

[13] F. Bornebroek, "TWINSCAN scanner evolution Enabling 5000 wafers per day," *ASML Images*, Fall Edition 2008.

[14] M. A. Van Den Brink, J. P. H. Benschop and E. R. Loopstra, "DUAL STAGE LITHOGRAPHIC APPARATUS AND DEVICE MANUFACTURING METHOD". US Patent 7161659 2007.

[15] X. Lu and I.-u.-r. Usman, "A NOVEL LONG-STROKE PLANAR MOTOR," in *ASPE 26th Annual Meeting*, vol. 52, pp. 143-146, 2011.

[16] C. M. M. van Lierop, J. W. Jansen, A. A. H. Damen, and P. P. J. van den Bosch, "Control of multi-degree-of-freedom planar actuators," *IEEE International Conference on Control Applications*, pp. 2516-2521, 2006.

[17] I.-u.-r. Usman, Long Stroke Magnetic Levitation Planar Stages (PhD's Thesis), Vancouver: University of British Columbia, 2015.

[18] W. Kim and D. L. Trumper, "High-precision magnetic levitation stage for photolithography," *Precision Engineering*, vol. 22, no. 2, pp. 66-77, 1998.

[19] D. L. Trumper, M. E. Williams and T. H. Nguyen, "Magnet arrays for synchronous machines," *IEEE Industry Applications Society Annual Meeting*, vol.1, pp. 9-18, 1993.

[20] I.-u.-r. Usman and X. Lu, "Force Ripple Attenuation of 6-DOF Direct Drive Permanent Magnet Planar Levitating Synchronous Motors," *IEEE Transactions on Magnetics*, vol. 51, no. 12, pp. 1-8, 2015.

[21] H. A. Haus and J. R. Melcher, Electromagnetic Fields and Energy, 1 ed., Englewood Cliffs: Prentice-Hall, Inc., 1989.

[22] J. W. Jansen, J. L. G. Janssen, J. M. M. Rovers, J. J. H. Paulides and E. A. Lomonova, "(Semi-) analytical models for the design of high-precision permanent magnet actuators," *International Compumag Society Newsletter*, vol. 16, no. 2, pp. 4-17, 2009.

[23] G. Akoun and J.-P. Yonnet, "3D analytical calculation of the forces exerted betwen two cuboidal magnets," *IEEE Transactions on Magnetics*, vol. MAG-20, no. 5, pp. 1962-1964, 1984.

[24] J. W. Jansen, C. M. M. van Lierop, E. A. Lomonova and A. J. A. Vandenput, "Modeling of magnetically leviated planar actuators with moving magnets," *IEEE Transactions on Magnetics*, vol. 43, no. 1, pp. 15-25, 2007.

[25] Q. Han, C. Ham, R. Phillips, "Four-and eight-piece Halbach array analysis and geometry optimization for Maglev," *IEEE Proceedings-Electric Power Applications*, vol. 152, no. 3, pp. 535-542, 2005.

[26] W. Kim, High-precision planar magnetic levitation (PhD's Thesis), Boston: Massachusetts Institute of Technology, 1997.

[27] H. H. Woodson and J. R. Melcher, Electromechanical dynamics, 1968.

[28] J. W. Jansen, E. A. Lomonova, A. J. A. Vandenput and J. C. Compter, "Design tool for a 6-dof planar motor with moving permanent magnets and standstill coils," in *Proceedings of the 4th International Symposium on Linear Drives for Industry Applications*, vol. 8, no. 10, 2003.

[29] H-W. Lee, S. G. Lee, S.-H. Won and J. Lee, "Optimal design of high-precision maglev system using simulation-based DOE and FEM," *IEEE Proceedings Electric Power Applications*, vol. 153, no. 5, pp. 773-779, 2006.

[30] P. Jin, Y. Yuan, H. Lin, S. Fang and S.L. Ho, "General analytical method for magnetic field analysis of Halbach magnet arrays based on magnetic scalar potential," *Journal of Magnetics*,vol. 18, no. 2, pp. 95-104, 2013.

[31] H. Allag, J. P. Yonnet and M.E. H. Latreche, "3D analytical calculation of forces between linear Halbach-type permanent-magnet arrays," in *Advanced Electromechanical Motion Systems & Electric Drives Joint Symposium, 2009. ELECTROMOTION 2009. 8th International Symposium on*, pp. 1-6, IEEE, 2009.

[32] M. Dyck, Magnetically levitated six degree of freedom micro-machining rotary table (Master's Thesis), Vancouver: University of British Columbia, 2014.

[33] X. Lu, N. Rao and I.-u.-r. Usman, "Six-axis position measurement system for levitated motion stages," *CIRP Annals - Manufacturing Technology*, vol. 62, no. 1, pp. 507-510, 2013.

[34] K. Maguire, Multi-Degree of Freedom Position Sensor for Planar Motor (Master's Thesis), Vancouver: University of British Columbia, 2015.

[35] X. Li, W. Gao, H. Muto, Y. Shimizu, S. Ito and S. Dian, "A six-degree-of-freedom surface encoder for precision positioning of a planar motion stage," *Precision Engineering*, vol. 37, no. 3, pp. 771-781, 2013.

Appendices

Appendix A

A.1 3D Magnetic Field Simulation for 2D Pattern I

To address the problem of 2D magnet pattern in Binnard's design [9] when applying to magnetically levitated planar motor, 3D magnetic field is calculated by 3D analytical model developed in this thesis, which is shown in figure A.1.

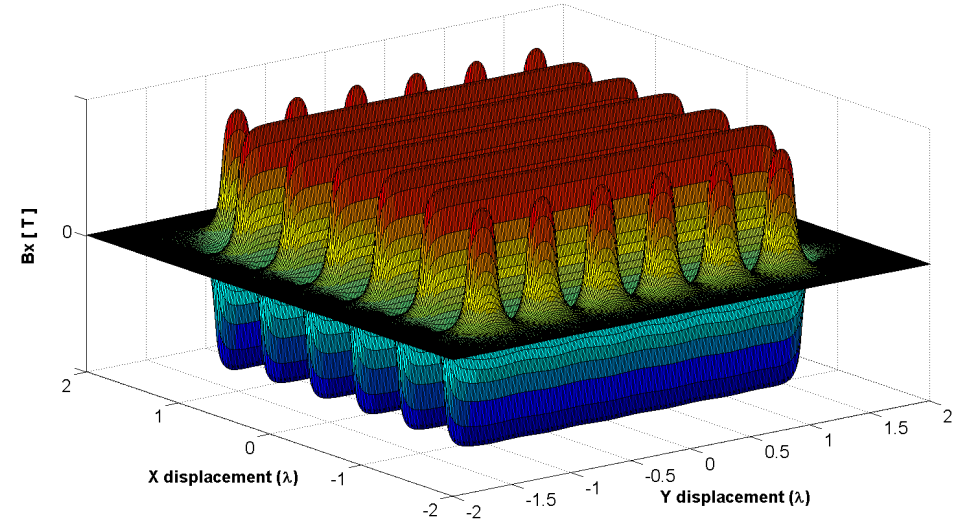

(a) Magnetic flux density in x axis at z=-1mm

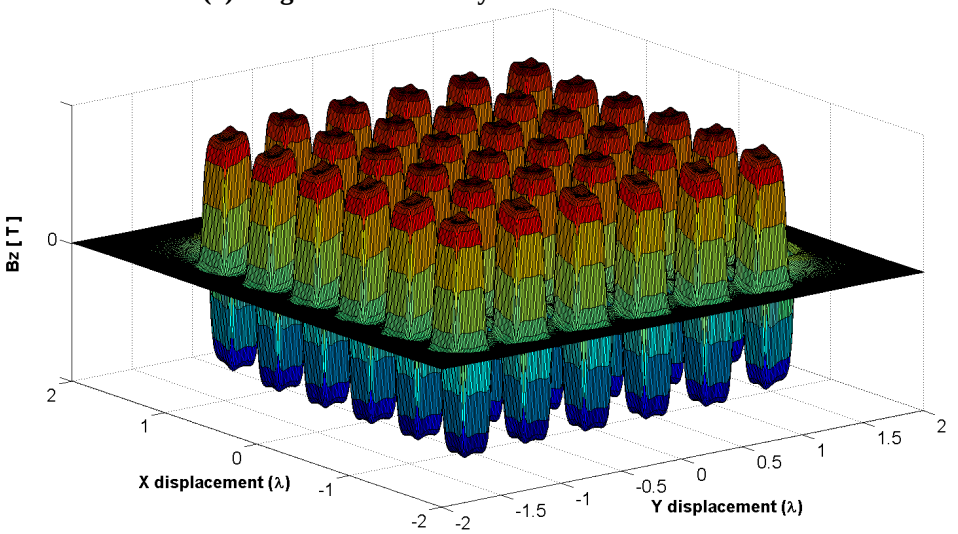

(b) Magnetic flux density in z axis at z=-1mm

Figure A.1 3D analytical model of Binnard's design [9]

A.2 3D Magnetic Field Simulation for 2D Pattern II

Similar as section A.1, 3D magnetic field of Computer's design in [11] is calculated as shown in figure A.2.

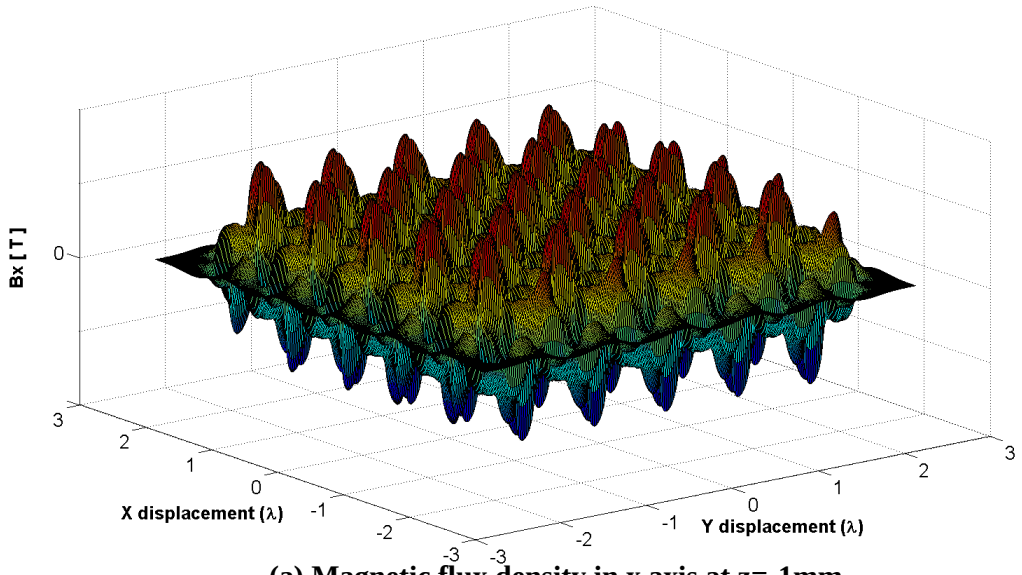

(a) Magnetic flux density in x axis at z=-1mm

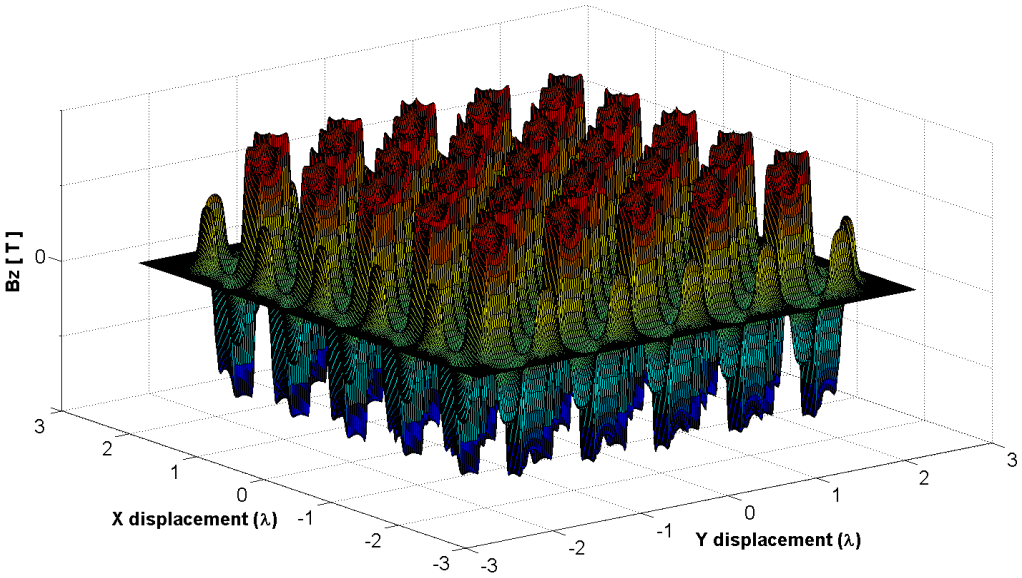

(b) Magnetic flux density in z axis at z=-1mm

Figure A.2 3D analytical model of Compter's design [11]

Appendix B

B.1 Single Layer Surface Charge Model

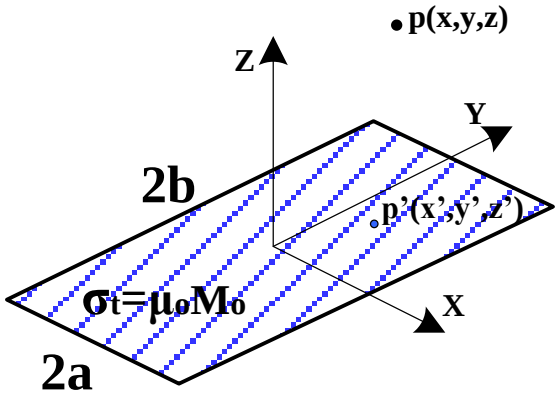

Figure B.1 Single layer surface charge model

Substituting (2.16) into $B = \mu_0 H$, it follows that

$$B(\vec{r}) = \int_{S'} \frac{\sigma_m(\vec{r'})(\vec{r} - \vec{r'})da'}{4\pi\left|\vec{r} - \vec{r'}\right|^3} \qquad (0.1)$$

Since magnetic charge, $\sigma_t = \mu_0 M_0$, at top surface is uniform, it can be taken out of surface-integral, then (0.1) is simplified as

$$B(\vec{r}) = \sigma_t \int_{S'} \frac{(\vec{r} - \vec{r'})da'}{4\pi\left|\vec{r} - \vec{r'}\right|^3} \qquad (0.2)$$

In Cartesian coordinates, $\vec{r} - \vec{r'}$ and $\left|\vec{r} - \vec{r'}\right|$ are written by

$$\vec{r} - \vec{r'} = (x - x')\vec{i} + (y - y')\vec{j} + (z - z')\vec{k} \qquad (0.3)$$

$$\left|\vec{r} - \vec{r'}\right| = \sqrt{(x - x')^2 + (y - y')^2 + (z - z')^2} \qquad (0.4)$$

Plugging (0.3) and (0.4) into (0.2) and setting $z' = 0$, yields

$$\vec{B} = \frac{\sigma_t}{4\pi}\int_S \frac{[(x-x')\vec{i} + (y-y')\vec{j} + z\vec{k}]da'}{(\sqrt{(x-x')^2 + (y-y')^2 + z^2})^3} = B_x\vec{i} + B_y\vec{j} + B_z\vec{k} \qquad (0.5)$$

For x component of $\vec{B}$, it follows that

$$B_x = \frac{\sigma_t}{4\pi}\int_{-b}^{b}\int_{-a}^{a} \frac{(x-x')dx'}{(\sqrt{(x-x')^2 + (y-y')^2 + z^2})^3} dy' \qquad (0.6)$$

By introducing two variables, $u = x - x'$ and $A = (y-y')^2 + z^2$ into (0.6), B_x is written by

$$B_x = \frac{\sigma_t}{4\pi}\int_{-b}^{b}\int_{-a}^{a} \frac{-udu}{(u^2 + A)^{\frac{3}{2}}} dy' \qquad (0.7)$$

After taking inside integration, it follows that

$$B_x = \frac{\sigma_t}{4\pi}\int_{-b}^{b} \frac{dy'}{\sqrt{(x-a)^2 + (y-y')^2 + z^2}} - \frac{\sigma_t}{4\pi}\int_{-b}^{b} \frac{dy'}{\sqrt{(x+a)^2 + (y-y')^2 + z^2}} \qquad (0.8)$$

Again, by introducing another three variables, $v = y - y'$, $M = (x-a)^2 + z^2$ and $P = (x+a)^2 + z^2$ into (0.8), yields

$$B_x = \frac{\sigma_t}{4\pi}\int_{-b}^{b} \frac{d(-v)}{\sqrt{(-v)^2 + M}} - \frac{\sigma_t}{4\pi}\int_{-b}^{b} \frac{d(-v)}{\sqrt{(-v)^2 + P}} \qquad (0.9)$$

After taking final integration of B_x, it follows that

$$\begin{aligned} B_x = {} & \frac{\sigma_t}{4\pi}\ln(\sqrt{(x-a)^2 + (y-b)^2 + z^2} - (y-b)) - \frac{\sigma_t}{4\pi}\ln(\sqrt{(x-a)^2 + (y+b)^2 + z^2} - (y+b)) \\ & - \frac{\sigma_t}{4\pi}\ln(\sqrt{(x+a)^2 + (y-b)^2 + z^2} - (y-b)) + \frac{\sigma_t}{4\pi}\ln(\sqrt{(x+a)^2 + (y+b)^2 + z^2} - (y+b)) \end{aligned} \qquad (0.10)$$

Denotes $S = x - (-1)^i a$, $T = y - (-1)^j b$ and $R = \sqrt{S^2 + T^2 + z^2}$, then B_x can be written by

$$B_x = \frac{\sigma_t}{4\pi}\sum_{i=0}^{1}\sum_{j=0}^{1}(-1)^{i+j}\ln(R-T) \qquad (0.11)$$

Similarly, for y component of $\vec{B}$, it can be written by

$$B_y = \frac{\sigma_t}{4\pi}\sum_{i=0}^{1}\sum_{j=0}^{1}(-1)^{i+j}\ln(R-S) \qquad (0.12)$$

For z component of $\vec{B}$,

$$B_z = \frac{\sigma_t}{4\pi}\int_{-b}^{b}\int_{-a}^{a}\frac{z dx' dy'}{((x-x')^2+(y-y')^2+z^2)^{\frac{3}{2}}} \qquad (0.13)$$

by plugging u, v and A into (0.13), B_z can be simplified as

$$B_z = \frac{\sigma_t}{4\pi}\int_{-b}^{b} z\int_{-a}^{a}\frac{d(-u)}{(u^2+A^2)^{\frac{3}{2}}}d(-v) \qquad (0.14)$$

After taking inside integration, it follows that

$$B_z = \frac{\sigma_t}{4\pi}\int_{-b}^{b}\frac{z(x-a)dv}{(v^2+z^2)\sqrt{v^2+z^2+(x-a)^2}} - \frac{\sigma_t}{4\pi}\int_{-b}^{b}\frac{z(x+a)dv}{(v^2+z^2)\sqrt{v^2+z^2+(x+a)^2}} \qquad (0.15)$$

By introducing four new variables, $R_0 = \sqrt{v^2+z^2+(x-a)^2}$, $R_1 = \sqrt{v^2+z^2+(x+a)^2}$ $t_0 = \frac{(x-a)v}{zR_0}$ and $t_1 = \frac{(x-a)v}{zR_1}$, into (0.15), then B_z can be further simplified as

$$B_z = \frac{\sigma_t}{4\pi}\int_{-b}^{b}\frac{dt_0}{1+t_0^2} - \frac{\sigma_t}{4\pi}\int_{-b}^{b}\frac{dt_1}{1+t_1^2} \qquad (0.16)$$

After taking integration on the right side of above equation, and rearrange final expression, it follows that

$$B_z = \frac{\sigma_t}{4\pi}\sum_{i=0}^{1}\sum_{j=0}^{1}(-1)^{i+j}tg^{-1}\frac{ST}{zR} \qquad (0.17)$$